Electron and X-ray Beam Control in Laser Wakefield Acceleration

Gustafsson, Cornelia

2025

Document Version:
Publisher's PDF, also known as Version of record

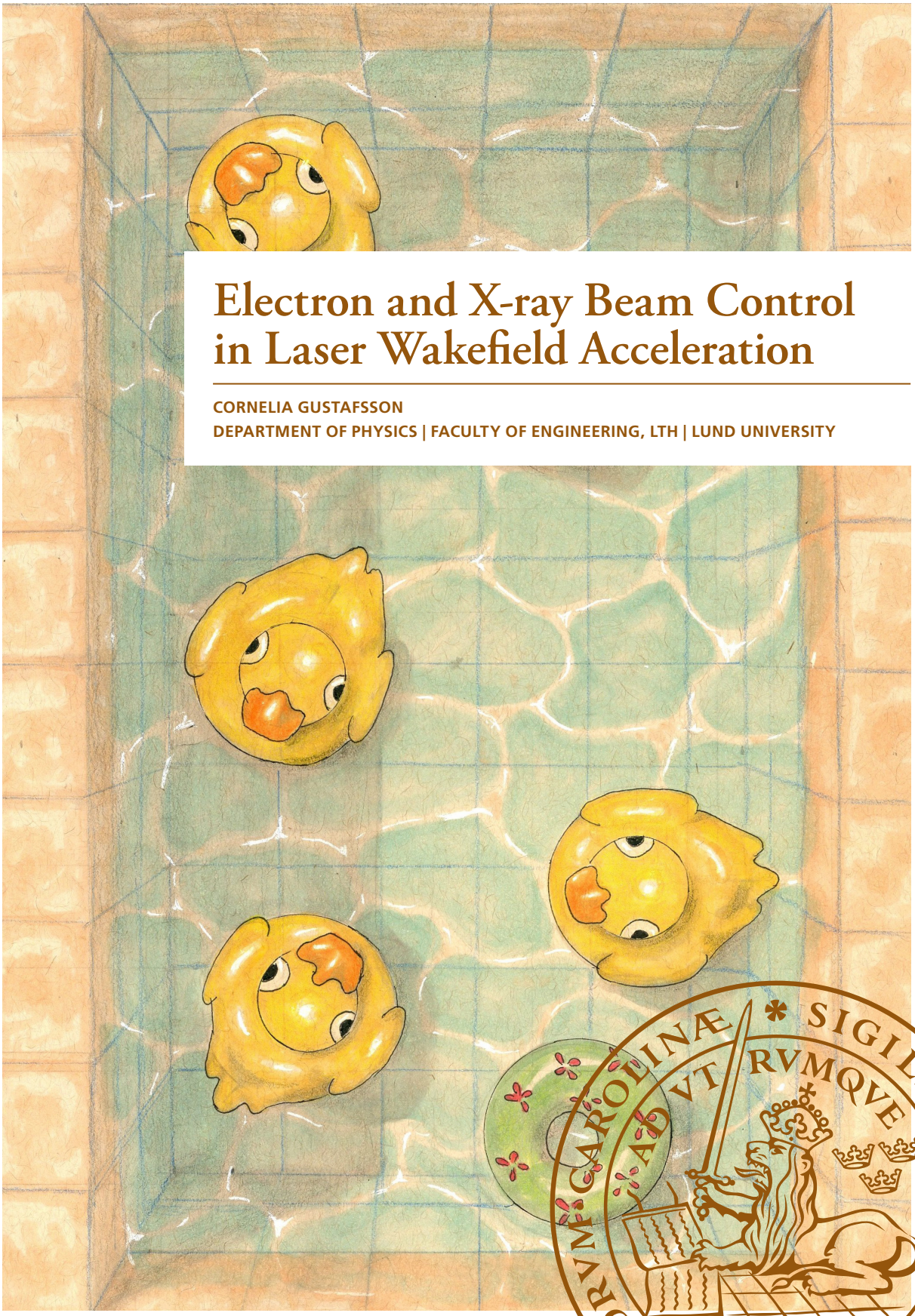

Electron and X-ray Beam Control in Laser Wakefield Acceleration

CORNELIA GUSTAFSSON
DEPARTMENT OF PHYSICS | FACULTY OF ENGINEERING, LTH | LUND UNIVERSITY

Electron and X-ray Beam Control in Laser Wakefield Acceleration

Cornelia Gustafsson

LUND
UNIVERSITY

Akademisk avhandling som för avläggande av teknologie doktorsexamen vid tekniska fakulteten vid Lunds universitet kommer att offentligen försvaras den 11 juni 2025, kl 9.15 i Rydbergssalen, på Fysiska institutionen, Professorsgatan 1, Lund.
Fakultetsopponent: Dr. Arie Irman
Helholtz-Zentrum Dresden-Rossendorf, Tyskland

Academic dissertation which, by due permission of the Faculty of Engineering at Lund University, will be publicly defended on June 11, 2025, at 9.15 a.m. in the Rydberg Lecture Hall, at the Department of Physics, Professorsgatan 1, Lund, for the degree of Doctor of Philosophy in Engineering.
Faculty opponent: Dr. Arie Irman
Helmholtz-Zentrum Dresden-Rossendorf, Germany

Organization
LUND UNIVERSITY

Atomic Physics
Department of Physics
P.O. Box 118
SE-221 00 Lund
Sweden

Document name
DOCTORAL DISSERTATION

Date of disputation
June 11th, 2025

Sponsoring organization

Author(s)
Cornelia Gustafsson

Title and subtitle
Electron and X-ray Beam Control in Laser Wakefield Acceleration

Abstract

This thesis focuses on the optimization and control of laser-driven plasma-based acceleration, which involves the driver laser pulse, the accelerated electrons and the subsequent generation of x-rays.

In laser wakefield acceleration (LWFA), a high-power laser pulse, typically with terawatt-level power, is focused tightly into a gas, reaching intensities on the order of $> 10^{18}$ W/cm^2. Even at the leading edge of the pulse, the gas becomes fully ionized, so the main part of the pulse interacts primarily with plasma. The relativistic ponderomotive force expels plasma electrons from the high-intensity region, creating a void, or wake, just behind the laser pulse. Within this ion cavity, the charge separation generates strong electric fields on the order of TV/m, enabling electrons injected into the cavity to be accelerated to hundreds of MeV over just a few millimeters. Various injection schemes allow for control over the energy and energy spread of the electron bunch. However, producing monoenergetic electron bunches remains a significant challenge, and some energy spread is always present. The maximum achievable energy is limited by dephasing, the distance over which electrons gain energy before being decelerated.

The ion cavity is nearly spherical, resulting in strong radial fields. Consequently, electrons are not only accelerated along the laser's propagation direction, but also oscillate transversely about the optical axis. These oscillations lead to the emission of x-ray radiation. However, because of this motion, electrons exiting the cavity exhibit a large divergence, and the resulting x-rays inherit this broad angular spread.

This thesis addresses each of these limitations. By tailoring the plasma density profile at the start of the acceleration process, the energy spread of the electron bunch can be reduced. The usage of a high-density plasma lens significantly decreases electron beam divergence across a broad energy range. Within this lens, electron deflection results in x-ray emission with a divergence approaching the incoherent limit. Furthermore, by introducing a high-density region at the end of the acceleration stage, it becomes possible to extend the maximum energy gain beyond the conventional dephasing limit of LWFA.

Key words
Laser Wakefield Acceleration, LWFA, laser plasma acceleration, particle acceleration, x-ray applications, x-ray, tomography, beam steering, electron acceleraion, plasma lens, plasma reconstruction, Abel inversion, low-divergence, beam steering

Classification system and/or index terms (if any)

Supplementary bibliographical information

Language
English

ISSN and key title
0281-2762, Lund Reports on Atomic Physics, LRAP 610

ISBN
print: 978-91-8104-513-0
pdf: 978-91-8104-514-7

Recipient's notes

Number of pages
154

Price

Security classification

Signature _____ Date 11 June 2025

Electron and X-ray Beam Control in Laser Wakefield Acceleration

Cornelia Gustafsson

Doctoral Thesis
2025

LUND
UNIVERSITY

Electron and X-ray Beam Control in Laser Wakefield Acceleration

Department of Physics
Faculty of Engineering
Lund University

Lund Reports on Atomic Physics, LRAP 610 (2025)
ISBN (print): 978-91-8104-513-0
ISBN (pdf): 978-91-8104-514-7

Igenom regnbågar och krockade bilar
Springer det vilsna själar som aldrig rostar

Krockade bilar - Vånna inget

Abstract

This thesis focuses on the optimization and control of laser-driven plasma-based acceleration, which involves the driver laser pulse, the accelerated electrons and the subsequent generation of x-rays.

In laser wakefield acceleration (LWFA), a high-power laser pulse, typically with terawatt-level power, is focused tightly into a gas, reaching intensities on the order of $> 10^{18}$ W/cm^2. Even at the leading edge of the pulse, the gas becomes fully ionized, so the main part of the pulse interacts primarily with plasma. The relativistic ponderomotive force expels plasma electrons from the high-intensity region, creating a void, or wake, just behind the laser pulse. Within this ion cavity, the charge separation generates strong electric fields on the order of TV/m, enabling electrons injected into the cavity to be accelerated to hundreds of MeV over just a few millimeters. Various injection schemes allow for control over the energy and energy spread of the electron bunch. However, producing monoenergetic electron bunches remains a significant challenge, and some energy spread is always present. The maximum achievable energy is limited by dephasing, the distance over which electrons gain energy before being decelerated.

The ion cavity is nearly spherical, resulting in strong radial fields. Consequently, electrons are not only accelerated along the laser's propagation direction, but also oscillate transversely about the optical axis. These oscillations lead to the emission of x-ray radiation. However, because of this motion, electrons exiting the cavity exhibit a large divergence, and the resulting x-rays inherit this broad angular spread.

This thesis addresses each of these limitations. Tailoring the plasma density profile at the start of the acceleration process, allows the energy spread of the electron bunch to be reduced. The usage of a high-density plasma lens significantly decreases electron beam divergence across a broad energy range. Within this lens, electron deflection results in x-ray emission with a divergence approaching the incoherent limit. Furthermore, by introducing a high-density region at the end of the acceleration stage, it becomes possible to extend the maximum energy gain beyond the conventional dephasing limit of LWFA.

Populärvetenskaplig sammanfattning

Partikelacceleratorer, som går tillbaka till 1920-talet, har långsiktigt bidragit till medicin och forskning. En konventionell accelerator består av en metallstruktur och använder elektriska fält för att accelerera partiklarna, dvs öka deras hastighet. För att uppnå extremt hög energi i partiklarna krävs mycket starka fält, men extrema nivåer leder till att metallstrukturen skadas genom jonisering av ytan. Därför måste acceleratorer byggas mycket stora för att kunna nå riktigt hög partikelenergi. Elektroner är en typ av partiklar som kan accelereras och genom processen kan de generera röntgenstrålning.

En alternativ metod till en konventionell accelerator är en laserdriven plasmaaccelerator. Här sker acceleration i ett redan fullt joniserat plasma, vilket möjliggör extremt kraftiga accelerationsfält. Detta betyder att en sådan accelerator kan göras hela 10 000 gånger mer kompakt än den konventionella typen, vilket gör den tillräckligt liten för att rymmas i ett vanligt forskningslaboratorium och ger enklare tillgång till högenergetiska partiklar och röntgenstrålning. Denna teknologi är möjlig tack vare utvecklingen av lasrar med extremt korta ljuspulser, med extremt hög ljusintensitet. När laserpulsen tränger igenom plasmat, trycks dess elektroner undan, vilket lämnar ett elektronfattigt område bakom pulsen. Precis som när en motorbåt kör på stilla vatten. Där, i plasmavågen, skapas starka accelerationsfält i laserpulsens färdriktning, som snabbt kan accelerera elektroner till hastigheter nära ljusets hastighet och därmed mycket höga energier. Då elektronerna accelereras producerar de röntgenstrålning. Eftersom att laserpulsen är kort får även elektron- och röntgenstrålning liknande längd, vilket leder till intensiva strålar som möjliggör tidsupplösta studier av ultrasnabba fenomen.

En laserpuls som interagerar med ett plasma får en något lite lägre hastighet jämfört med farten i vakuum. När lasern genererar en plasmavåg, får även denna lite lägre hastighet. Elektroner däremot,

snabbt relativistiska, kan nå hastigheter nära laserpulsen i vakuum. Så småningom hinner de ikapp laserpulsen i plasmat och börjar då sakta ner. Detta utgör en av de största begränsningarna för en laserdriven plasmaaccelerator. Den nästan sfäriska plasmavågen skapar även kraftiga radiella fält som fokuserar elektroner mot vågcentrum och tvingar dem att oscillera. Under dessa oscillationer sänds röntgenstrålning ut i framåtriktningen. Som ett resultat får de elektroner som lämnar acceleratorn stor utbredning i rummet och liknande utbredning ses i röntgenstrålen, vilket begränsar antalet användningsområden något.

I denna avhandling har strålegenskaperna hos en laserdriven plasmaaccelerator förbättrats med flera metoder. De experimentella metoderna utnyttjar högeffektslasern vid Lunds universitet och tillhörande högeffektslaboratorium. Experimentet sker i vakuum och kräver avancerade optiska metoder för att kunna kontrollera och få en glimt av vad som sker i plasmat. En metod använder en plasmalins som, likt accelerationsplasmat, tål extremt kraftiga elektriska och magnetiska fält. Den består av ett andra plasma som placeras direkt efter plasmaacceleratorn. Inuti linsen bildas starka radiella fält, och det är de magnetiska fälten som fokuserar elektronstrålarna från acceleratorn, vilket drastiskt minskar deras spridning. Genom fokuseringen länkas elektronerna av, och genom denna avlänkning avger de röntgenstrålning. På grund av elektronernas mycket höga energi, och att de enbart tillåts att länkas av en gång i linsen, leder till att röntgenstrålningen från elektronerna i linsen har en mycket liten spridning, mindre än den från acceleratorn. De här elektron- och röntgenstrålarna, nu med mycket liten spridning, gör att strålningen lämpar sig utmärkt i tillämpningsområden som kräver strålar av högre intensitet. Ett exempel är för att studera snabba reaktioner i varma material. De här strålarna kan också transporteras över större sträckor, vilket ökar tillämpningsområdena. Detta då effektiviteten av transporten ökar om strålen behåller en så liten spridning som möjligt.

Med ett extra plasma går det också att accelerera elektroner över längre sträckor. Det här plasmat designas så att plasmavågen verkar röra sig snabbare i framåtriktningen, och följer med de accelererade elektronerna. Elektronerna befinner sig då i en accelererande del av plasmavågen under en längre tid innan de hinner ikapp laserpulsen, vilket gör att toppenergin inte längre begränsas av detta. Dessa framsteg ökar de potentiella användningarna för laserdrivna plasmaacceleratorer och är därför betydande för forskning som utnyttjar dem.

Popular science summary

Particle accelerators have been around since the 1920s and have been an important tool in medicine and research ever since. A conventional accelerator is made up of a metallic structure, and strong fields accelerate the electrons to high energies by increasing their velocity. To reach extreme energies, very strong fields are needed, but the extreme-field strengths lead to the breakdown of the metallic structure by ionizing the surface. The accelerators are therefore made large so that high particle energies are reached. A particle that can be accelerated is electrons, and from them x-rays are generated.

An alternative to a conventional accelerator is the laser-driven plasma accelerator. In this case, the acceleration takes place in a plasma, which is already ionized, enabling extremely high accelerating fields. This means that the accelerator can be reduced by 10,000 times compared to the conventional accelerator, which in turn makes it small enough to fit in a standard research laboratory. This technology is possible because of the development of extremely short-pulsed lasers that can reach extreme intensities. When the laser pulse plows through the plasma, the plasma electrons are expelled away from the pulse. Just behind it, a region devoid of electrons is formed, similar to when a powerboat runs on water. In that plasma wave, extreme accelerating fields in the same direction as the laser propagation are created. These fields quickly accelerate the electrons to velocities approaching the speed of light and corresponding energies. As electrons are accelerated, x-rays are produced. Because of the short pulse duration of the laser pulse, the electron beam and subsequent x-rays have a similar duration and result in intense beams. These ultrashort beams make ultrafast time-resolved measurements possible.

A laser pulse that is interacting with a plasma will slow down as opposed to its vacuum speed. When the laser pulse excites the plasma wave, the wave propagation slows down together with the laser pulse. The electrons, on the other hand, have a relativistic speed, similar to

the laser pulse in vacuum. Eventually, they outrun the laser pulse in the plasma and, as a result, they slow down. This phenomenon is one of the greatest limitations of laser-driven plasma accelerators. The almost spherical plasma wave generates strong radial fields which focus the electrons toward the center of the wave, where they will oscillate. During these oscillations, x-rays are emitted in the forward direction. As a result of these oscillations, the electrons leaving the accelerator have a large spatial spread, and the x-rays will have a similar spread. This somewhat limits the possible applications.

In this thesis, the radiation created by the laser-driven plasma accelerator has been improved by using several different methods. The experimental methods use the high-power laser at Lund University and the high-power laser laboratory. The experiment takes place in vacuum and requires advanced optical methods to control and diagnose the plasma interaction. One method uses a plasma lens that, similar to the accelerator's plasma, can sustain extreme electric and magnetic fields. The lens consists of a second plasma that is positioned immediately after the plasma accelerator. In the lens, strong radial fields are created, which focus the accelerated electrons and significantly reduce their spread. Through the process of being focused, the electrons radiate x-rays. Because of the electrons' high energies and the restriction to only one deflection within the lens, these x-rays have a small transverse spread, much smaller than that from the accelerator. These electrons and x-rays, now with a tiny spread, make them suitable for experiments which require intense beams, for example, to study fast reactions in warm materials. These small beams are also more efficiently transported, which increases the possible applications. This is possible since the beam transport efficiency increases when they maintain the smallest spread possible.

An extra plasma can also be used to extend the acceleration. This plasma is designed in such a way that the plasma wave seems to propagate faster and follow the accelerated electrons. As a consequence, the electrons remain within an accelerating part of the wave over a longer time before they outrun the laser and are thus accelerated to higher energies. These improvements potentially increase the usage of laser-driven plasma accelerators and are important for research areas that use them.

List of Publications

This thesis is based on the following publications, which are referred to by their Roman numerals.

I **Combined plasma lens and rephasing stage for a laser wakefield accelerator**
C. Gustafsson, E. Löfquist, K. Svendsen, A. Angella, A. Persson and O. Lundh.
Scientific reports **14**, 26286 (2024).

II **Collimated x-rays emitted through laser-driven plasma lensing**
C. Gustafsson, E. Löfquist, J. Björklund Svensson, A. Angella, K. Svendsen, A. Persson and O. Lundh.
Accepted for publication in IOP conference proceedings.

III **Plasma density profile reconstruction of a gas cell for ionization induced laser wakefield acceleration**
F. Filippi, L.T. Dickson, M. Backhouse, P. Forestier-Colleoni, C. Gustafsson, C. Cobo, C. Ballage, S. Dobosz Dufrénoy, E. Löfquist, G. Maynard, C.D. Murphy, Z. Najmudin, F Panza, A. Persson, M. Scisció, O. Vasilovici, O. Lundh, and B. Cros.
Journal of instrumentation **18**, C05013 (2023).

IV **Parametric study of low-divergence x-ray generation from a laser-plasma accelerator using an overdense plasma lens**
C. Gustafsson, A. Angella, E. Löfquist, J. Björklund Svensson, A. Persson and O. Lundh.
Manuscript in preparation.

V **Correlating optical pulse-front tilt steering of X-ray and electron pulses from laser wakefield accelerators**
E. Löfquist, C. Gustafsson, A. Angella, A. Persson, and O. Lundh.
Manuscript in preparation.

VI **Spatiotemporal distribution of liquid mass from spray M using x-ray tomography driven by a laser plasma accelerator**
E. Löfquist, B. Lehnert,C. Gustafsson, A. Angella, A. Persson, O. Lundh, and E. Berrocal.
In review, Submitted to Physics of Fluids.

Abbreviations

BBO	Barium Borate
BS	Beam Splitter
CCD	Charge-Coupled Device
CMOS	Complementary Metal Oxide Semiconductor
CPA	Chirped Pulse Amplification
DC	Direct Current
FEL	Free-Electron Laser
FFT	Fast Fourier Transform
fs	femtosecond
FWHM	the Full Width at Half Maximum
IFFT	Inverse Fast Fourier Transform
LLC	Lund Laser Centre
LWFA	Laser Wakefield Acceleration
OAP	Off-Axis Parabolic mirror
PFT	Pulse-Front Tilt
PL	Plasma Lens
rf	radio frequency
S/N	Signal-to-noise ratio
STC	Spatiotemporal couplings
TW	Terawatt

Contents

Papers

Chapter 1

Introduction

Since their establishment in the 1920s [1, 2], accelerators have been vital in both fundamental research and cancer therapy. Today, more than 30,000 different machines exist worldwide, with different geometries and sizes ranging from table-top sources to several kilometers in length. Fully 97% of all accelerators are in commercial use and in hospitals, while a mere 3% are used in research. Accelerators are used to reach high particle energies, where the final energy depends on the desired usage, ranging from a few eV to GeV range. Accelerated electrons are also used in x-ray production, which have a wide range of applications.

The final particle energy is dependent on the strength of the accelerating field and the travel distance of the particles. Increasing the accelerating field requires a higher radio frequency (rf) amplitude. Because acceleration takes place within a metallic cavity, the rf-field strength is limited by the material's breakdown potential, beyond which electrons are ripped off the surface, causing permanent damage. Thus, the accelerators must be large to allow for sufficient energy gain. The most extensive accelerator is Europe's 27 km Large Hadron Collider [3]. At MAX IV in Lund, electrons reach 3 GeV via a 300 m linear accelerator. Given their size, alternatives such as Laser Wakefield Acceleration (LWFA) offer suitable table-top complements.

In 1979, Tajima and Dawson [4] demonstrated theoretically and via simulations that electrons could be accelerated to 10 GeV over 30 cm with a terawatt (TW) laser pulse in plasma. The benefit of using a plasma is that it is already ionized and thus lacks breakdown potential. As the laser pulse propagates through the plasma, a wake formation is self-sustained behind the laser pulse. The laser pulse achieves a high phase velocity as it travels through the plasma, sustaining a consistent wake. Unlike the traditional rf cavity, plasma can endure extremely high field strengths, enabling a drastic size reduction of accelerators. Initially, the generation of sufficiently powerful laser pulses for this accelerator

was not feasible. The situation improved with the invention of chirped pulse amplification (CPA) [5], an advancement recognized by the 2018 Nobel Prize in Physics. In 1995, Modena *et al.* [6] at Rutherford Appleton Laboratory managed to accelerate electrons using the Vulcan laser, but a significant breakthrough for LWFA occurred in 2004. Three separate teams [7–9] demonstrated that through matching the laser pulse duration and spot size with the plasma they could reliably accelerate quasi-monoenergetic electron bunches. This acceleration happens within the *bubble regime*, a non-linear wave structure generated by the laser pulse as it moves through the plasma [10, 11].

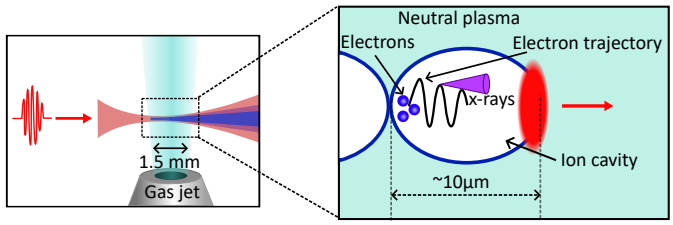

Figure 1.1. *A conceptual sketch of the LWFA process. A high-power laser pulse is focused at the beginning of a gas jet, here with an orifice of 1.5 mm which resembles the jet used in the experiments presented in this thesis. The laser pulse ionizes the gas and excites a nonlinear plasma wave, in which electron can be accelerated and subsequent x-ray radiation emitted. The accelerating structure is about* 10µm *and co-propagate behind the laser pulse throughout the length of the jet.*

The principle of LWFA is shown in Figure 1.1. An experimental setup usually utilizes a supersonic gas jet, with a low Z-number gas, such Helium. In the figure, a high-power laser pulse is focused at the beginning of a gas jet. Already at the leading edge of the laser pulse, the Helium gas is fully ionized, creating a plasma and subsequent wakefield. As the intense laser pulse propagates through the plasma, the electrons are expelled away from the high-intensity regions, leaving a void behind the laser pulse, similar to a cavity. Within this cavity, the field gradients are of an order of magnitude of TV/m, and electrons able to break into this wave, or "catch" it as a surfer riding a wave, will be exposed to high accelerating fields whithin it and quickly accelerate to relativistic energies. During their excursion within the wake, the oscillatory motion will lead to the emission of x-ray radiation.

Since its breakthrough, LWFA has been used repeatedly to produce high-energetic electron bunches, and the development has followed that of high-power lasers [12]. Achieving the necessary power, typically at TW, requires laser pulses in the femtosecond (fs) range. This brief interaction with plasma results in accelerated electron bunches and x-ray radiation of equivalent duration [13, 14]. Such femtosecond electron bunches open up new applications in materials science, including the

investigation of electron dynamics on the fs time scale [15].

The refractive index of the plasma is different from that of the vacuum, c, leading to the group velocity of the laser pulse being less than the speed of light in vacuum. The electron bunch, on the other hand, has a speed approaching c. After a certain distance, the electrons will outrun the laser pulse and be exposed to a decelerating field. This *dephasing* is one of the greatest limitations to the maximum particle energies achievable by the LWFA. Within their own frame, the electrons inside the bubble move in all directions, with strong transverse oscillations, which causes a large transverse divergence of the electron bunch upon exiting the acceleration. This limits possible beam transport and applications of the electron bunch.

The electron oscillation during LWFA is similar to that of an undulator, but where the plasma determines the oscillation period instead of bending magnets. At the largest transverse acceleration, the relativistic electrons will radiate x-rays, with a synchrotron-like spectrum. This insight allows for the application of existing synchrotron and undulator theories to radiation produced via LWFA. The compact source size of radiation is advantageous for the imaging of small structures [16] and phase contrast imaging methods [17]. Moreover, the fs duration of x-rays makes them suitable for probing ultrafast events within the dense state of materials [18–21]. However, by the same principle as for the electrons, the strong oscillations will cause the x-rays to have a large divergence, leading to a frequent limitation of the signal-to-noise ratio (S/N) at the sample and detection plane. This is overcome by averaging over data acquisitions at the cost of the ultra-fast resolution.

This thesis focuses on beam control related to LWFA, which involves the laser pulse, electron bunch, and x-ray beams. The main part utilizes two gas jets – the first one for the LWFA, and the second as a plasma lens to manipulate the electron bunch and subsequent x-ray radiation.

Boosting to overcome dephasing

In this thesis, a second gas jet is placed immediately after the first jet responsible for the LWFA. It is configured so that the plasma density is higher than for LWFA. This principle will cause the whole wave structure to shift and follow the speed of the electron bunch. As a consequence, the electrons are kept continuously in an accelerating phase and overcome the energy limit set by the dephasing [22].

Plasma lenses for LWFA electrons

Charged particle optics, such as quadrupoles, are to this day challenging to use in combination with LWFA. This thesis explores the use of plasma optics as an alternative to magnets. Capable of sustaining strong

magnetic fields, the plasma effectively manipulates electron bunches [23]. This plasma lens is also a second gas jet, configured in a similar way as when it is used for energy boosting. Compact and experimentally simple, the plasma lens enhances beam profiles crucial for an LWFA seeded free-electron laser (FEL) [24].

Generation of narrow x-ray beams

The strong magnetic fields inside the LWFA will cause electrons to emit x-rays with a large divergence. Using a plasma lens, the strong electron deflection will cause an additional radiation event. Within the plasma lens, the highly relativistic electrons are deflected so the radiation is mainly in the forward direction, and the bending radius is greater than the length of the lens, restricting the electron motion to a partial oscillation. The divergence of these x-rays is less than that produced by LWFA by itself and approaches the incoherent limit. Producing such x-rays can enhance beam transportation, given that most x-ray optics rely on the incidence angle, thus improving the S/N at the detection plane.

Beam pointing control

The CPA relies on efficient compression of the laser pulse to reach high-power laser pulses. The principle presented in this thesis utilizes multiple passes between reflective gratings. If the gratings are misaligned with respect to each other, the laser pulse will have coupled temporal and spatial aberrations. These types of aberrations lead to steering of the electron bunch and x-rays produced through LWFA [25]. In the work presented in this thesis, these are introduced in a controlled way, demonstrating the importance of beam control for subsequent staging and applications.

1.1 Thesis outline

This thesis focuses on improving LWFA development through laser pulse and plasma optimization. It comprises four principal chapters: Chapter 2 briefly surveys high-power lasers and the relevant systems utilized in this research. Chapter 3 covers plasma physics with a foundation in electrodynamics, detailing the experimental diagnostic methods for plasma analysis used here. Chapter 4 integrates content from the previous chapters to explain LWFA with emphasis on injection and acceleration, and concludes with the generation and use of x-rays. Chapter 5 discusses beam optimization for manipulating LWFA electrons, producing low-divergence x-rays, and beam pointing control. Chapter 6 summarizes the results and provides future perspectives.

Chapter 2

High-power lasers

Achieving the non-linear interaction necessary for LWFA between a laser pulse and plasma demands an ultra-short laser pulse on the fs scale, with energy high enough to produce pulse powers in the TW range. These powerful pulses can be focused to reach intensities of the order of magnitude of 10^{19} W/cm^2, entering the relativistic regime. To reach these parameters, CPA is implemented, illustrated in Figure 2.1. A laser pulse is stretched in time and frequency before it is amplified. This alleviates the damage threshold of the gain medium as the energy density is reduced. After the amplification stage, the pulse is compressed to fs duration so that a high pulse power is reached. This chapter provides an overview of high-power laser pulses and details two laser systems located at the Lund Laser Centre (LLC). The first part introduces electromagnetic waves in the context of LWFA. Then the laser systems at the LLC High-Power Laser Facility are presented, beginning with the Titanium Sapphire laser, which is capable of producing 2 J laser pulses with a duration of 35 fs, centered at a wavelength of 800 nm. The chapter then discusses the high-power OPCPA laser system, which is designed to produce sub-10 fs laser pulses with an energy output of 250 mJ and a center wavelength of 780 nm.

2.1 Electromagnetic waves

The following explains fundamental elements of electromagnetic and Gaussian waves to comprehend laser-plasma interactions. The fundamental basis of classical electromagnetic waves and their interaction with media is described by a set of first-order partial differential equations, known as the Maxwell equations [26]:

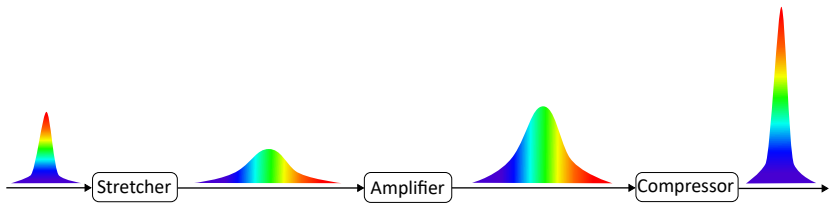

Figure 2.1. *Illustration of CPA. A laser pulse is generated from the oscillator, and is then stretched in time and frequency. Then it enters one or more amplification stages to increase the energy per pulse. Once the desired energy is reached, the pulse is compressed in time and frequency, so that a high-power laser pulse is achieved.*

$$\begin{aligned} \nabla \cdot \mathbf{B} = 0, \quad \nabla \times \mathbf{E} + \frac{\partial \mathbf{B}}{\partial t} = 0 \\ \nabla \cdot \mathbf{D} = 0, \quad \nabla \times \mathbf{H} - \frac{\partial \mathbf{D}}{\partial t} = 0 \end{aligned} \tag{2.1}$$

where $\mathbf{B}$ represents the magnetic flux, $\mathbf{E}$ denotes the electric field, $\mathbf{D}$ is the electric displacement, and $\mathbf{H}$ is the magnetic field. When the fields exhibit harmonic time variations, expressed as $e^{-i\omega t}$ with ω being the central frequency, $\mathbf{E}$ and $\mathbf{B}$ fulfill the Helmholtz equation:

$$(\nabla^2 + \mu\epsilon\omega^2) \begin{bmatrix} \mathbf{E} \\ \mathbf{B} \end{bmatrix} = 0 \tag{2.2}$$

if the propagation vector takes the form $\mathbf{k} \cdot \mathbf{k} = k^2 \mathbf{n} \cdot \mathbf{n} = \mu\epsilon\omega^2$, where μ is the permeability and ϵ the permittivity. From these two parameters, the phase velocity of light in any medium is defined:

$$v = \frac{\omega}{k} = \frac{1}{\sqrt{\mu\epsilon}} = \frac{c}{n}, \tag{2.3}$$

where c is the speed of light in vacuum and $n = \sqrt{\mu\epsilon/(\mu_0\epsilon_0)}$ is the refractive index. The constants μ_0 and ϵ_0 are the permeability and permittivity of vacuum, respectively.

Within the framework of electrodynamics, it is beneficial to utilize vector and scalar potentials [26, 27]. The vector field $\mathbf{A}$ allows us to represent the magnetic flux through the equation $\mathbf{B} = \nabla \times \mathbf{A}$. By incorporating this into the second top equation of eq. (2.1), the expression can be reformulated as follows:

$$\nabla \times \left(\mathbf{E} + \frac{\partial \mathbf{A}}{\partial t} \right) = 0 \Rightarrow \mathbf{E} = -\frac{\partial \mathbf{A}}{\partial t} - \nabla\phi \tag{2.4}$$

where a curl of a gradient scalar field is always zero, $\nabla \times (\nabla\phi) = 0$. The vector and scalar field reduce the solution to eq. (2.1) from four independent equations to two. In scenarios where the source of the wave is absent, such as in the LWFA detailed in Chapter 4, the scalar potential becomes $\phi = 0$. Consequently, the electric field is determined purely by the vector potential, expressed as $\mathbf{E} = -\partial\mathbf{A}/\partial t$. A plane wave represents one of the solutions to eq. 2.2, and its electromagnetic field is given by $\mathbf{E} = E_0 \exp(i\mathbf{kx} - i\omega t)$, described using the vector field:

$$\mathbf{A} = \frac{A_0}{\omega} \exp(i\mathbf{k}\cdot\mathbf{x} - i\omega t) \tag{2.5}$$

where $A_0 = E_0\omega$ denotes the amplitude of the vector field. In the context of LWFA, this parameter frequently characterizes the strength of the interaction between the laser pulse and the plasma. Thus, it is advantageous to normalize A_0/ω with respect to the motion of the electron quiver [28], resulting in the following:

$$a_0 = \frac{A_0 q_\mathrm{e}}{\omega^2 m_\mathrm{e} c} = \frac{E_0 q_\mathrm{e}}{\omega m_\mathrm{e} c}, \tag{2.6}$$

where m_e is the rest mass of the electron and q_e the elementary charge. This parameter directly relates the energy of a laser pulse to the response of the material.

Although the concept of an ideal plane wave aids in understanding the formal framework for electromagnetic waves, it cannot be used to excite the nonlinear plasma wave necessary for LWFA, as discussed in Chapter 4. To reach relativistic intensities required for LWFA, approximately 10^{19} W/cm^2, a high-power laser pulse must be tightly focused. This requires an inhomogeneous laser pulse, which is modeled by a Gaussian laser pulse characterized by a radius $r = \sqrt{x^2 + y^2}$, traveling in the z direction. Similarly to the plane wave, the Gaussian wave is a solution to eq. (2.2) [29].

$$\mathbf{E}(\mathbf{r}, t) = E_0 \left(-\mathbf{x} + \frac{x}{z + iz_0}\mathbf{z}\right) U(\mathbf{r}, t) \tag{2.7}$$

where $U(\mathbf{r}, \mathbf{t})$ is the complex amplitude, which also satisfies eq. (2.2), $\nabla^2 U + k^2 U = 0$. For an ideal Gaussian laser pulse with negligible spatiotemporal couplings, the spatial and temporal parts of eq. (2.7) can be decoupled, $U(\mathbf{r}, t) = U(r) \cdot U(t)$. Thus, the time-dependent spatial complex amplitude can be described by:

$$\begin{aligned} U(r,t) =& \mathfrak{A}_0 \frac{W_0}{W(z)} \exp\left(\frac{-r^2}{W^2(z)}\right) \exp\left(-ikz - ik\frac{r^2}{2R(z)} + i\zeta(z)\right) \times \\ & \exp\left(-\frac{t^2}{\tau^2} + i\omega t\right) \end{aligned} \tag{2.8}$$

where $\mathfrak{A}_0$ is an arbitrary complex amplitude. $W(z) = W_0\sqrt{1+(z/z_0)^2}$ is the radius of the beam where the intensity has dropped by 86% in position z away from the minimum waist, $W_0 = \sqrt{\lambda z_0/\pi}$. $R(z) = z(1+(z/z_0)^2)$ is the beam curvature, and $\zeta(z) = \arctan(z/z_0)$ the Gouy phase. These parameters are needed to fully describe the Gaussian beam spatially. However, for a certain wavelength λ, if one of the above parameters is known, the rest can be determined. The duration of the pulse, with a center wavelength, ω, is determined by τ, which is 86% of the temporal width of the pulse, related to the FWHM through $\tau_{FWHM} = \tau\sqrt{2\ln(2)}$.

The theoretically shortest possible pulse duration is given by the time-frequency product, and for a Gaussian laser pulse this is:

$$\tau_{FWHM}\Delta\nu = 0.44. \tag{2.9}$$

where $\Delta\nu$ is the pulse frequency bandwidth in Hz. A laser pulse that meets this criterion is considered transform-limited. The bandwidth in this context is defined by the gain bandwidth of the laser medium. In the real scenario, the pulse duration is longer than the transform-limited pulse. However, this shows that a short pulse duration requires a broad gain bandwidth. The on-axis peak intensity of a Gaussian laser pulse is determined by:

$$I_0 = \frac{2\mathcal{E}}{\tau\pi W_0^2}, \tag{2.10}$$

where $\mathcal{E}$ is the pulse energy. Eq. (2.6) is usually expressed in terms of I_0, since generally $I_0 \propto |E_0|^2$. The normalized vector potential, a_0, can thus be treated as a key design parameter for LWFA:

$$a_0 = \frac{q_\mathrm{e}}{\omega m_\mathrm{e}}\left(\frac{2I_0}{\epsilon_0 c^3}\right)^{1/2}. \tag{2.11}$$

In practical units, this is expressed as $a_0 \approx 0.85\sqrt{I_0[10^{18}\mathrm{W/cm^2}]}\lambda[\mu\mathrm{m}]$, where λ is the center wavelength of the laser pulse. For the Ti:Sapphire laser pulse described here, focused by the $f/13$ off-axis parabolic (OAP) mirror, as illustrated in Figure 2.3, $I_0 \approx 1.5\times10^{19}$ W/cm^2, and the normalized vector potential amplitude becomes $a_0 \approx 2.6$. In Chapter 4, the consequences of a_0 for LWFA is discussed in more detail.

2.2 Lund High-Power Laser Facility

The High-Power Laser Facility is located at LLC. For many years, the multi-TW Ti:Sapphire CPA laser was the workhorse of the facility and responsible for the research output presented in this thesis, Papers I–VI.

In 2024, the system was replaced by a novel multi-TW barium borate (BBO) optical parametric chirped pulse amplification (OPCPA) system.

2.2.1 The multi-TW Ti:Sapphire CPA laser

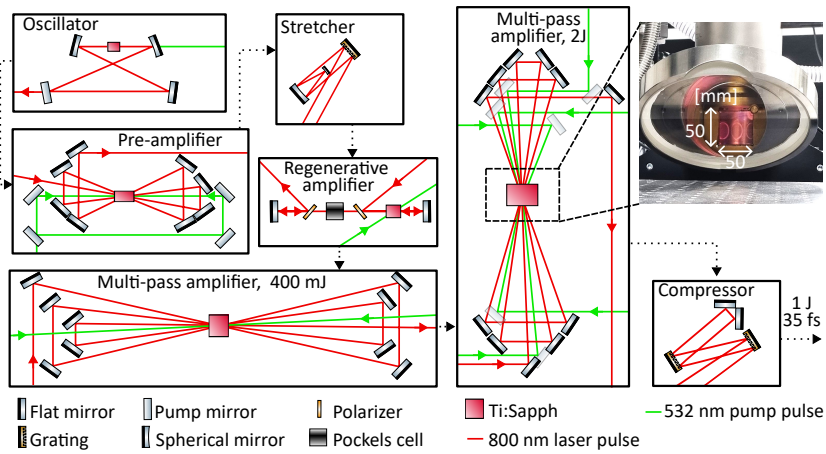

Figure 2.2. *A schematic illustration of the main parts of the Ti:Sapphire laser system. The oscillation starts by pumping the Ti:Sapphire crystal within the oscillator with a 532 nm diode laser. Active mode-locking generates laser pulses with an 80 MHz repetition rate. The pulse repetition rate is then reduced to 10 Hz and propagates to the pre-amplifier, then the stretcher, then to the regenerative amplifier, and then the first multi-pass amplifier. Before the second multi-pass amplifier, 100 mJ are split off and amplified in the final stage, and then propagates to the grating compressor. The inset shows a photograph of the final Ti:Sapphire crystal situated in a cryogenically cooled vacuum chamber.*

The Ti:Sapphire CPA laser system is divided into four main components: oscillator, stretcher, amplification, and compression. Figure 2.2 illustrates a schematic view of the whole laser system, indicating the output energy after each amplification stage. In the oscillatory stage, a Ti:Sapphire crystal is optically pumped by a 532 nm diode laser. Using active mode-locking, the system generates short pulses at a frequency of 80 MHz. After the oscillator, the laser pulses pass through a pulse picker, reducing the repetition rate to 10 Hz, before entering the pre-amplification stage, which enhances the pulses' temporal contrast by suppressing amplified spontaneous emission (ASE). Significant ASE ionizes the LWFA's target gas before the main pulse arrives, disrupting the process. It is therefore important to minimize the ASE intensity. After the pre-amplification stage, the pulse propagates to the stretcher, where it is stretched temporally and spectrally using a

grating and a demagnifying telescope. Following this, at the regenerative amplifier stage, the pulse undergoes 10 round trips before the Pockels cell is activated to rotate the phase of polarization by π radians and extract the laser pulses. Afterward, the pulse proceeds to the first multi-pass amplifier, attaining a final energy of 400 mJ while operating at 10 Hz. Subsequently, 25% of this pulse is directed to the final amplification phase, where its energy increases from 100 mJ to 2 J, and the repetition rate is reduced to 5 Hz. The inset of Figure 2.2 shows the Ti:Sapphire crystal within a vacuum chamber, cooled to cryogenic temperatures to minimize thermal lensing effects. At highest power, experiments operate in single-shot mode to prevent thermal lensing as even the 5 Hz repetition rate results in too high energy dissipation in the crystal. Due to multiple amplification stages, temporal stretching alone does not suffice to keep the pulse intensity below the gain medium's damage threshold. Hence, the pulses are also expanded in beam diameter between the amplifiers. In the last amplification stage, the pulse reaches a FWHM of approximately 22 mm, to optimally fit the final Ti:Sapphire crystal sized 50×50 mm and 30 mm in length, and is amplified to 2 J. Before compression, the pulses need further expansion to about 60 mm in FWHM to stay below the damage threshold of the gold gratings in the compressor. During compression, the power is so high that the rest of the beam path, including the compressor, must be kept in a vacuum. The laser pulse is powerful enough to trigger nonlinear interactions with the air, which degrades the pulse duration and power. The pulse that ultimately reaches the experimental chamber has a duration of 35 fs, with an energy of approximately 1 J. Throughout most experiments in this thesis, the pulse duration is slightly longer, around 38 fs, and the energy on target ranges from 0.7 to 0.9 J.

The experimental setup

After the pulse compression, the entire experiment must be kept in vacuum, to preserve pulse quality. A sketch of the experiment is shown in Figure 2.3. This configuration, with some slight modifications, was utilized in Papers I–VI. The laser pulse enters the vacuum chamber from below and before arriving at the f/13 off-axis parabolic mirror (OAP), a small fraction of the laser pulse wing is picked up by an elliptic mirror and serves as a probe pulse (represented by the orange line). The probe pulse is synchronized with the laser pulse using a delay stage. Before diagnostics, the probe is divided with a 50:50 beamsplitter to capture the shadowgraphic image and interference pattern, which aids in plasma diagnosis. The primary laser pulse can proceed to the gas jet for LWFA, or a pick-up mirror may be placed in its path to redirect the beam toward laser diagnostics along the red dashed route. Outside the chamber, the beam can either be directed to the wavefront sensor for pulse characterization or to the focus camera for assessment

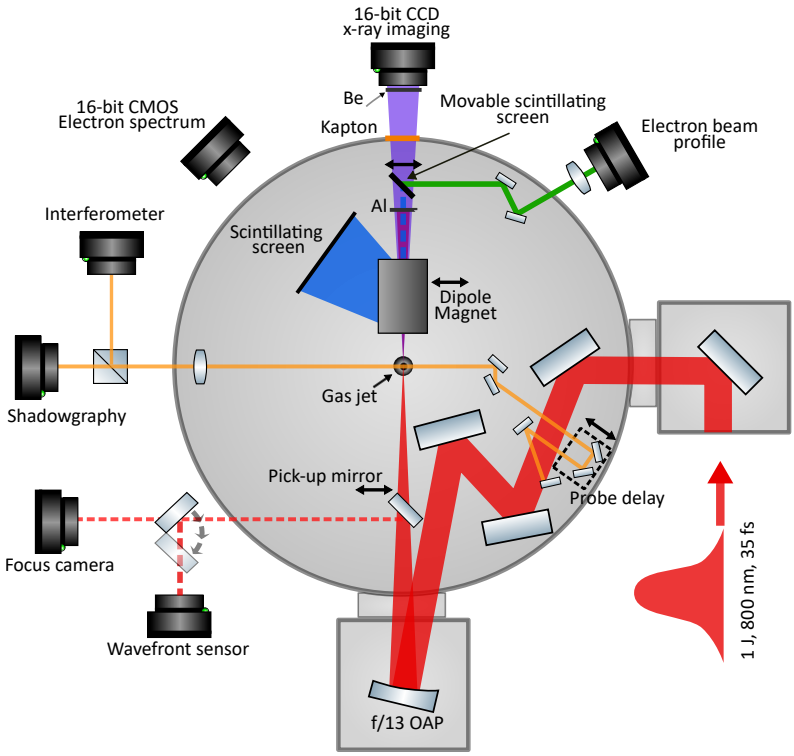

Figure 2.3. *A schematic sketch of the experimental setup, used with minor modifications in papers I-VI. The compressed laser pulse enters from below and propagates to the f/13 OAP mirror. The gas target, illustrated as a gas jet, is situated in the center of the chamber. Before the OAP, a portion of the wing of the laser pulse is picked up and used as a temporally synchronized probe pulse (orange). Alternative beam paths are indicated with dashed lines. The dipole magnet can be moved in and out of place to retrieve the electron spectrum (in) and electron beam profile (out). The in-position of the magnet, together with the scintillating screen and 16-bit CMOS forms the electron spectrometer.*

of the focal spot. The wake excitation is heavily dependent on the pulse transverse quality, and wavefront aberrations, such as coma and astigmatism. The wavefront aberrations redistribute the laser pulse intensity, causing inefficient coupling between the laser pulse and plasma [30]. To reach the needed intensities for an efficient LWFA, the wavefront aberrations must be minimized. This is done with the wavefront sensor and adaptive optics in a closed-loop iteration. The adaptive optics is located upstream of the experimental chamber, not shown in Figure 2.3.

From the gas jet, three femtosecond beams emerge – the now slightly depleted laser pulse, an electron bunch (blue), and x-rays (purple). The remaining laser pulse energy is blocked after the dipole magnet with a

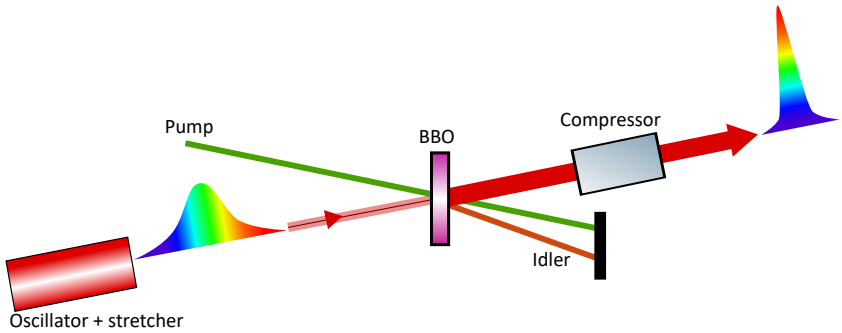

Figure 2.4. *A sketch showing the principles of OPCPA. The oscillator both generates the seed and stretches the pulse, which propagates to a non-linear medium (BBO), where the pump amplifies the seed through optical parametrization. From the process, an auxiliary beam emerges, called an idler. The amplified seed is then compressed in the compressor.*

3 µm Al-foil. The electron bunch can propagate through the 0.83 T dipole magnet, so they are deflected on a scintillating screen (Lanex Regular [31]), where the electrons will induce a phosphorescence that is imaged by the 16-bit CMOS. The dipole magnet, scintillating screen, and 16-CMOS constitute the electron spectrometer, since the deflection of the electrons depends on their acquired energy during acceleration. The x-rays continue in the forward direction from the interaction, propagate through a 50 µm Kapton window that seals the vacuum, through a 250 µm Be protecting the back-illuminated deep depletion CCD-chip. This x-ray camera is used both to characterize the energy of the x-ray radiation and to do x-ray imaging.

When the dipole magnet is moved out from the beam path, the electrons instead propagate to a second scintillating screen (blue dashed path and movable scintillating screen) without being deflected. Thus, the scintillation corresponds to the transverse beam profile of the electron bunch. The beam profile is imaged by a 12-bit CMOS camera outside the chamber (green path). Note that the x-ray diagnostics are disabled and moved out of the beam path when the beam profile is studied to protect the x-ray camera from unnecessary radiation.

2.2.2 The OPCPA laser

The optical parametric chirped pulse amplification (OPCPA) technique is based on parametric conversion of the laser pulse. Unlike traditional CPA, which relies on gain in a laser medium, OPCPA uses parametric amplification in a nonlinear crystal, offering a broader bandwidth and faster amplification without thermal effects. Since the amplification takes place without a gain medium, there is no ASE, immediately rendering a high temporal contrast, which reduces the preionization of the plasma

and enhances the reproducibility and control in LWFA. The principle is illustrated in Figure 2.4. Stretching and oscillation occur simultaneously at the same location. The stretched seed pulse travels through a nonlinear medium, in this case BBO, where the seed is amplified. The degree of this amplification depends on the phase matching between the pump and the seed. Phase matching is fulfilled if the total phase velocity is conserved, so that $\Delta k = 0$, where $\Delta k = k_{out} - \sum k_{in}$ and k are the vectors of each component k, described by eq. (2.3). Any residual such that $\Delta k \neq 0$ leads to losses or inefficient parametrization. Three beams emerge from this process: the amplified seed, the residual pump, and an idler, with the latter being photons generated to satisfy both energy conversion and phase-matching conditions.

Table 2.1. *Summary of the properties of the Ti:Sapphire laser system and the OPCPA laser system. The experimental repetition rate refers to the capacity the LWFA experiment has been and is currently running at. Future upgrade of the OPCPA LWFA experiments involves acquisition at 10 Hz.*

System	Energy	Pulse duration	Repetition rate	Experimental repetition rate
Ti:Sapph	2 J	35 fs	10 Hz	Single shot
OPCPA	250 mJ	< 10 fs	10 Hz	Only tested at for single shot

In 2024, the multi-TW Ti:Sapphire laser system was replaced by a state-of-the-art OPCPA system, which has two output arms - one delivering 50 mJ, sub-10 fs pulses, at a 100 Hz repetition rate, and the other 250 mJ, sub-10 fs pulses at 10 Hz. The low energetic arm is used in extreme ultraviolet experiments, whereas the high energetic arm is used for the LWFA experiments. Table 2.1 details the specifications for these two laser systems. Although current experimental data are acquired on a single-shot basis, future plans for the LWFA experiment include an upgrade to a 10 Hz repetition rate.

Chapter summary

This chapter outlines the theoretical background of high-intensity laser pulses relevant to LWFA and describes the key laser systems at Lund Laser Centre: the multi-TW Ti:Sapphire laser system, with its well-established performance, and the recently installed OPCPA system, designed for sub-10 fs multi-TW operation. The next chapter introduces plasma physics underlying the acceleration process in more detail.

Chapter 3

Plasma theory and methods

Plasma, characterized by positive ions and free electrons, is a state of matter and is the most prevalent form in the universe, though relatively uncommon on Earth. Like other states of matter, plasma generally maintains electrical neutrality. In LWFA, the high field gradients needed to accelerate the electrons to GeV energies over distances on the cm-scale is possible due to the lack of breakdown potential within the plasma, since plasma consist of free electrons. However, material properties change with the state of matter, and the change in refractive index causes the laser pulse to evolve during the interaction. As will be discussed in Chapter 4, this is often beneficial. The pulse dispersion will depend on the plasma oscillations as well, which is detrimental for short laser pulses. For a full control of the acceleration process, it is crucial to diagnose the plasma density, and this is implemented in this thesis by probing the plasma transverse to the laser propagation axis, and imaging phase change with a folded interferometer. This chapter establishes the essential plasma theory needed to understand LWFA and introduces various methods used for its diagnosis.

3.1 Index of refraction of the plasma

The strength of an interaction between light and matter depends on the collective oscillations of the electrons, which is denoted the polarization density, $P = \epsilon_0 \chi \mathbf{E}(\mathbf{x}, t)$, where the dielectric constant is $\epsilon/\epsilon_0 = 1 + \chi$ and χ is the susceptibility. To arrive at the index of refraction, which is also governed by the collective oscillation of electrons, a simplified model for the dielectric constant can be applied [26]. Starting with the equation of

motion for one electron of charge $-q_e$, moving in the x coordinate due to an external field with frequency ω:

$$m_e(\ddot{\mathbf{x}} + \delta\dot{\mathbf{x}} + \omega\mathbf{x}) = -q_e\mathbf{E}(\mathbf{x}, t) \tag{3.1}$$

where δ is identified as a phenomenological parameter known as the damping constant. The displaced electrons give rise to a dipole moment. For a harmonic oscillating field, $\mathbf{E}(\mathbf{x}, t) \propto \exp(-i\omega t)$, it can be written as:

$$\mathbf{p} = -q_e\mathbf{x} = \frac{q_e^2\mathbf{E}(\mathbf{x}, \mathbf{t})}{m_e(\omega_b^2 - \omega^2 - i\omega\delta)}. \tag{3.2}$$

The binding frequency ω_b of an electron determines the resonances. At these frequencies, ionization can occur. In a plasma, the electrons are already ionized and the free electron ultimately has $\omega_b = 0$. Due to the short interaction time between the laser pulse and gas in an LWFA, the excitation happens adiabatically and the plasma can be treated collisionless, that is, cold and nonmagnetic. The damping constant is thus $\delta = 0$. Including these, the polarization density, given by the collective dipole moment, $P = n_e\mathbf{p}$, may therefore be expressed as:

$$P = -\frac{n_e e^2\mathbf{E}(\mathbf{x}, t)}{m_e\omega^2}. \tag{3.3}$$

The reduced polarization density, considering only the maximum induced oscillation, given by the amplitude of the electric field, yields $P/(\epsilon_0 E_0) = 1 + \chi$. Recalling that this is connected to the dielectric constant, the expression can now be written as:

$$\frac{\epsilon(\omega)}{\epsilon_0} = 1 - \frac{n_e q_e^2}{\epsilon_0\omega^2 m_e}. \tag{3.4}$$

In the expression, the dielectric constant now incorporates the dependence on frequency. A consequence of the frequency dependence of $\epsilon(\omega)$ is that laser pulses, which encompass multiple frequencies, are subject to dispersion. This means that the pulse will stretch as it propagates through a dispersive media, such as a plasma. In Chapter 2, the refractive index was derived as $n = \sqrt{\mu\epsilon/\mu_0\epsilon_0}$. In the case of nonmagnetic materials, the refractive index reduces to $n(\omega) = \sqrt{\epsilon(\omega)/\epsilon_0}$. Rearranging eq. (3.4) and applying $k = \omega\sqrt{\mu\epsilon}$, now leads to the dispersion relation of a cold, non-magnetized plasma:

$$\omega^2 = \omega_p^2 + k^2c^2, \tag{3.5}$$

where the plasma frequency is related to the plasma density through:

$$\omega_p = \left(\frac{n_e q_e^2}{\epsilon_0 m_e}\right)^{1/2}, \tag{3.6}$$

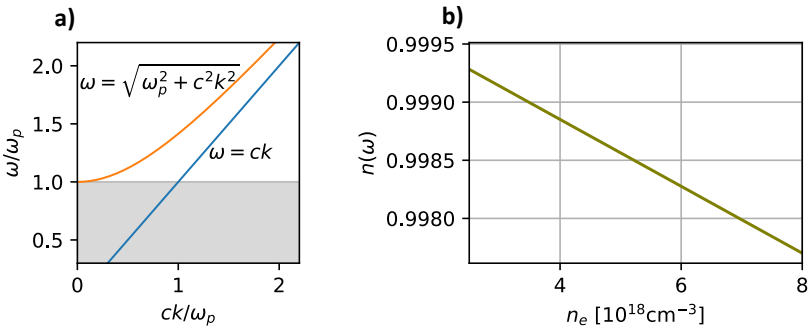

Figure 3.1. *In a) the dispersion relation of the plasma, where the gray-shaded area is where k only has imaginary solutions. The blue line represents the non-imaginary solutions to eq. (3.5), and the orange line is the light line. b) the refractive index of plasma for different plasma densities. The laser center frequency is kept constant at $\omega = 24 \times 10^{14}$ rad/s, corresponding to 800 nm.*

which is the fundamental frequency with which the electrons within in the plasma oscillate. The dispersion relation is illustrated in Figure 3.1a). The orange line is the real root of eq. (3.5), and the blue line is the light line, which corresponds to the vacuum propagation of light with frequency ω. From eq. (3.5), the refractive index of the plasma is also realized:

$$n(\omega) = \left(1 - \frac{\omega_\mathrm{p}^2}{\omega^2}\right)^{1/2}. \tag{3.7}$$

For a laser pulse with a wavelength centered at 800 nm, and for a plasma with a density of $n_\mathrm{e} = 4 \times 10^{18}$ cm^{-3}, the refractive index is $n \approx 0.9989$. Despite being nearly unity, this subtle deviation indicates that the phase velocity of light surpasses c within the plasma. Consequently, another implication is that the light will refract away from the surface normal of the medium, rather than towards it. The group velocity, on the other hand:

$$v_\mathrm{g} \equiv \frac{\partial \omega}{\partial k} = \frac{c^2}{\sqrt{c^2 + \omega_\mathrm{p}^2/k^2}} \tag{3.8}$$

is still less than c. For the same parameters as before, the group velocity is $v_\mathrm{g} \approx 0.9989c$. This mismatch in phase and group velocity means that there is slippage in phase as the laser propagates through the plasma. This effect becomes more prominent with increasing plasma density, illustrated in Figure 3.1 b). In the figure, the laser pulse frequency is kept constant at $\omega = 24 \times 10^{14}$ rad/s, corresponding to a wavelength of

800 nm. The range of the density and laser frequency are representative of typical experimental conditions presented within this thesis.

Eq. (3.5) has two nontrivial solutions for k: $\omega < \omega_\mathrm{p}$ and $\omega > \omega_\mathrm{p}$. In the first scenario, k assumes an entirely imaginary form, rendering the plasma opaque to ω, which results in the total reflection of the wave. In contrast, in the second scenario, k is real, which allows the plasma to become transparent to ω. Equation (3.6) delineates a direct correlation between plasma density and frequency, whereby these two regimes pertaining to the solutions to k are categorized as the *overdense* and *underdense* plasma regimes, respectively. When $\omega = \omega_\mathrm{p}$ occurs, a material parameter designated as *critical density* is obtained:

$$n_\mathrm{c} = \frac{\epsilon_0 m_\mathrm{e}}{q_\mathrm{e}^2}\omega^2. \tag{3.9}$$

This thesis, only considers the underdense regime, where $n_\mathrm{e} < n_\mathrm{c}$, as this is required for LWFA. The next chapter details the consequences of the differences in phase and group velocity.

3.2 Plasma diagnostics

The sensitivity of the acceleration process and the resultant radiation in LWFA to the overall set of acceleration parameters is attributable to its inherent nonlinear characteristics. The manipulation of laser pulse compression and wavefront is generally manageable, particularly with the application of sophisticated diagnostic tools. Furthermore, achieving comprehensive control over the accelerator is facilitated by the examination and diagnostic assessment of the plasma. A common method for diagnosing the plasma involves the use of a probe pulse, which is feasible due to the significant change in refractive index following the formation of the plasma channel. In this thesis, two main methods are used: the Nomarski interferometer and the modified Mach-Zehnder interferometer.

3.2.1 The Nomarski interferometer

The Nomarski interferometer [32–34] serves as an invaluable instrument for LWFA experiments due to its compactness. A temporally synchronized probe beam is used to image the gas jet or a gas cell with windows, traversing transversely to the primary laser pulse and subsequently directed to the interferometer, as shown in Figure 3.2. The plasma channel is imaged with a lens (L), with a focal length of f. A $\lambda/2$ plate, in conjunction with a polarizer (P1) at 45° to the optical axis, is utilized to create a circularly polarized pulse aligned with the polarization axis of the Wollaston prism. The Wollaston prism is composed of two birefringent crystals, which are cut at an angle α, facilitating the separation of the ordinary and extraordinary polarization states of the

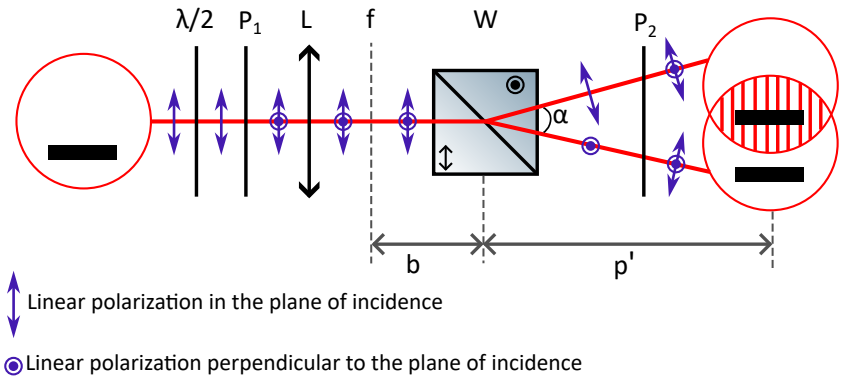

Figure 3.2. *Schematic of the principle of a Nomarski interferometer. The probe pulse propagates from left to right. Only part of the pulse covers the region of interest (black rectangle). The pulse propagates through a λ/2-plate, a polarizer (P1) and then through a lens (L) with a focal length of f, which images the region of interest. At the Wollaston prism (W), the two polarization states of the pulse are separated with an angle α. After the final polarizer (P_2), the pulse interferes with a spatially shifted copy of itself.*

laser pulse at the identical angle. In order to generate the interference pattern, an additional polarizer (P2) rotated at 45° is implemented after the Wollaston to create two equal and circular polarization states of the beam. These two replicas of the same beam will produce an interference pattern, provided that the angular spread ensures that the two beams coincide at the image plane, thus yielding an interference pattern with a fringe density of

$$i = \frac{\lambda}{\alpha}\frac{p'}{b}, \tag{3.10}$$

where b is the distance between the focal plane and the center of the prism, and p' is the distance from the prism to the image plane. The configuration of the beams ensures an overlap between the plasma channel and an undisturbed section of the beam, thereby inducing a phase shift in the interference pattern, viewed as a bend of the fringes. As α is usually fixed, the flexibility of the setup is determined by the distance between the lens and the prism. To accurately resolve the plasma, a high fringe density is needed, which facilitates small α, short b, and long p'. However, with shorter α, the image separation decreases for a certain lens, which may lead to overlapping regions of interest, making it impossible to distinguish the plasma channel. The prism thus needs to be chosen with the desired separation in mind, given a certain image magnification. The final image quality is determined by the lens system used together with the prism. Aberrations introduced by the lenses reduce the final fringe contrast.

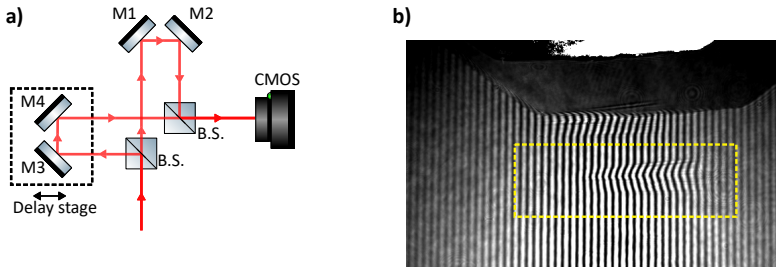

Figure 3.3. *a) The modified Mach-Zehnder interferometer. The probe pulse enters from the bottom and is split into a reference and probe beam at the first beam splitter (B.S.). The transmitted probe propagates to the first silver mirror (M1) in the forward direction and the reflected beam to the first mirror of the delay stage (M3). The one of the beams is slightly displaced transversely before they are recombined with the final B.S, such that a clear phase change along the plasma channel is visible, illustrated in b). The dashed yellow box highlights the region of interest used in the post-processing.*

3.2.2 The modified Mach-Zehnder interferometer

In Papers I–V, a principle similar to that of the Nomarski interferometer is implemented [35]. A limitation of the Nomarski interferometer is that the beamlet separation angle α and the fringe density i cannot be tuned independently of each other. With the modified Mach-Zehnder interferometer, or folded Mach-Zehnder as it is commonly called [35], the separation of the two beamlets and the fringe density can be adjusted independently, leaving an extra degree of freedom. However, unlike in the Nomarski interferometer, the two beamlets are not inherently synchronized, and the delay between the "reference" and the "probe beam" must be carefully aligned. In Paper III, this technique is combined with a shadowgraphic measurement to obtain an accurate single shot determination of the plasma density. The setup of the interferometer is shown in Figure 3.3 a) and the typical recorded image is shown in b). The probe beam enters from below in Figure 3.3a), and arrives at the first 50:50 beam splitter (B.S.). The reflected part propagates to a delay stage, with mirrors M3 and M4, while the transmitted beam propagates to mirrors M1 and M2. Both beams are recombined with the final beamsplitter, where the reflected beam delay is tuned to overlap temporally with the transmitted beam. One of the beams is displaced vertically to generate a clear plasma channel, shown in Figure 3.3b). In the figure, the fringe bend is only achieved when a phase difference is detected; that is, the region of interest overlaps with undisturbed plasma. The yellow box marks the region of interest used in the post-processing.

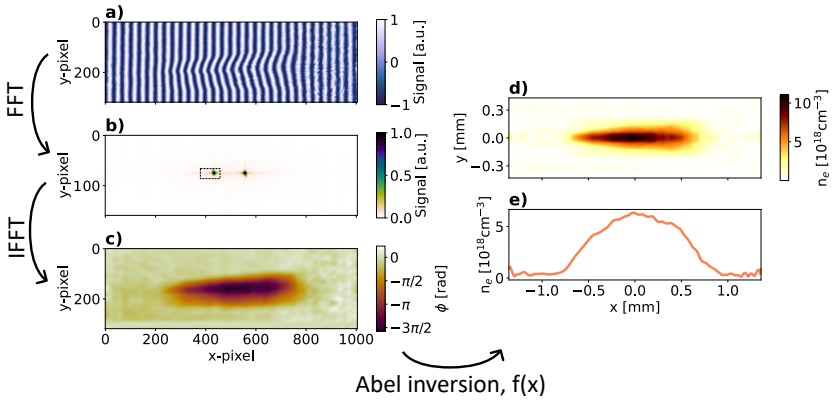

Figure 3.4. *The full procedure of the density retrieval algorithm. a) The raw image from 3.3 b) is cropped to capture only the region of interest, and the fringes are normalized to minimize the noise of the final retrieval. b) After the FFT, the image is filtered in the frequency domain (black dashed box). IFFT is applied to retrieve the 2D phase map in c). Abel inversion is used to retrieve the 3D phase, which can be converted to a density map, d). e) shows the weighted average of the density, essentially giving the density profile across the plasma channel.*

3.2.3 Phase retrieval and the Abel inversion

A common technique for phase retrieval of an LWFA experiment is the Abel inversion [35–37], which can be applied to cylindrically symmetric geometries. The forward transform converts an object in 3D space to the 2D space,

$$F(x) = 2\int_x^\infty \frac{f(r)r}{\sqrt{r^2 - x^2}}dr \tag{3.11}$$

while the inverse does the opposite,

$$f(r) = -\frac{1}{\pi}\int_r^\infty \frac{dF}{dx}\frac{dx}{\sqrt{x^2 - r^2}}. \tag{3.12}$$

There exists no analytical solution to eq. (3.12), but numerous numerical solvers. In cases of noisy and sparsely sampled data, certain solvers are inadequate to accurately reconstruct the 3D space. An approach that demonstrates computational efficiency and precision for sparse datasets is the "three-point" technique, which was used in Paper I, II, IV, and V [38]. The technique exploits the line-of-sight phase change created by underlying radial distribution. It interpolates three neighboring pixels during post-processing, making it robust towards noise. However, the interpolation technique may lead to the loss of sharp features of the plasma when this is present.

Due to the inherent symmetry around the laser axis of the plasma channel formed by an LWFA, the Abel inversion technique is frequently applied to reconstruct the 3D phase of the plasma channel from a 2D phase map, considering the laser axis as the axis of symmetry. In the context of a folded interferometer, the phase shift is correlated with the plasma density as outlined in [35]:

$$f(r) = \Delta\phi = \frac{2\pi}{\lambda} \int_L (n(\omega) - 1) dl. \tag{3.13}$$

With eq. (3.7), the density of the plasma channel as seen by the probe laser pulse with wavelength λ is:

$$n_e = n_c \left(1 - \left(\frac{\lambda \Delta\phi}{2\pi L} + 1 \right)^2 \right), \tag{3.14}$$

where L is the apparent length. Figure 3.4 shows the complete density retrieval algorithm. For both of the above-mentioned techniques, the phase is retrieved in post-processing from the interferometric images. A commonly used and straightforward phase-retrieval technique is the Fast Fourier Transform (FFT), which proves to be effective under conditions of high fringe density and minimal noise. The fringes depicted in Figure 3.4 a) have undergone normalization to enhance fringe contrast and mitigate some noise, resulting in suppression of the DC term within the Fourier domain, as shown in Figure 3.4 b). However, in scenarios where noise levels are substantial, the FFT tends to amplify the noise, and when combined with the Abel inversion, which is similarly based on the Fourier domain, the increased noise leads to inaccuracies in the extracted density [39, 40]. Although fringe normalization [41] can be applied to interferometric data to attenuate noise to some extent, this approach does not resolve issues related to fringe density, as these originate from the data retrieval process. In Figure 3.4 b), the black dashed box shows the filtered region. Most of the time, an asymmetrical filter is applied to reduce high-frequency noise. A filter that is too narrow will not adequately reconstruct the boundaries of the plasma density. Consequently, there is an inherent trade-off between noise reduction and accuracy. The fringes correspond to the wrapped phase. Following the application of filtering in the Fourier domain, inverse FFT (IFFT) is employed to retrieve the 2D phase, shown in c). The negative phase arises as a combination between fringe-bend direction and chosen region for filtering. For these particular data, the rightmost maxima in b) can be used to obtain a positive phase. However, both contain the same phase information, but the sign must be taken care of before the Abel inversion. Using the Python package *PyAbel* [38], the inverse Abel transform is then applied to the data to recover the 3D phase, with the density determined according to eq. 3.14. The density map is shown in d). Figure 3.4 e) shows the weighted average of the density in d), which essentially gives

the overall shape of the plasma channel. Note that if suitable fringe normalization is performed, an inverse cosine method may be utilized as an alternative to the Abel inversion. This methodology is based on the premise of cosine oscillation of the fringes [40].

Interferometric methods, like those discussed, are sensitive to fringe jumps. At larger phase changes exceeding 2π, that is, the distance between the fringe maxima or minima, it abruptly jumps to zero at 2π. Although post-processing can mitigate these effects, it adds extra uncertainty to data processing. An alternative method for density determination involves directly measuring phase shifts, for instance, using a wavefront sensor. This approach omits the need for FFT since it captures the 2D phase directly. The method's precision depends on the wavefront sensor's resolution and the post-processing accuracy. All probing techniques depend on the probe's propagation through the plasma, where high densities might refract the laser pulse strongly, causing it to miss the detector. In such scenarios, characterizing plasma at lower densities provides calibration data for extrapolation to higher densities.

Chapter summary

The interaction between the laser pulse and plasma is governed by the susceptibility of the plasma. As the refractive index drastically changes during the interaction, the laser pulse evolves such that the phase velocity slips and the group velocity increases. Diagnosis of the plasma is crucial for a complete picture of the nonlinear relativistic interaction between the plasma and the laser pulse in the LWFA. In this chapter, I have covered interferometric techniques for density reconstruction, which is an important experimental tool for plasma diagnosis. The next chapter explains why a dynamic change in the plasma refractive index plays a crucial role for efficient LWFA.

Chapter 4

Electron acceleration and x-ray generation

When exposed to the strong accelerating field present in LWFA, electrons achieve highly relativistic energies [42, 43], and off-axis oscillation leads to the emission of x-rays with a synchrotron-like spectrum. Since the LWFA breakthrough in 2004, significant advancements have been made in optimizing and controlling injection techniques. The laser-plasma interaction goes through the following steps: the target gas is ionized by the wing of the laser pulse, through field ionization, and electrons are exposed to the continuum. The main peak of the laser pulse thus interacts only with a plasma. Through the non-linear, relativistic ponderomotive force, the electrons are expelled from the high-intensity regions of the laser pulse, leaving a region devoid of electrons behind the drive laser pulse. The electrons are then injected into this void, focused radially, and accelerated longitudinally. This chapter is divided into three primary sections: the first discusses the basic principles of LWFA, the second examines the injection methods utilized in all the research papers forming the basis of this thesis, and the third delves into x-ray radiation.

4.1 The concept of LWFA

The principle of LWFA relies on nonlinear wave excitation, which is possible due to the nonlinear ponderomotive force. As an intense laser pulse plows through the plasma during its propagation, the electrons are expelled upward and backward away from the high intensity regions. The collective motion of electrons creates a sheath, and right behind

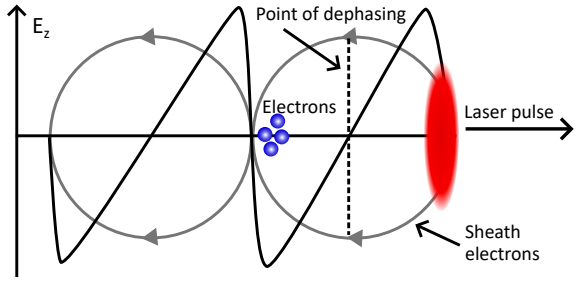

Figure 4.1. *Conceptual sketch of LWFA. The laser pulse propagates through the plasma, and by the relativistic ponderomotive force, the elctrons are expelled, upward and backward from the propagation direction, creating sheath. Right behind the laser pulse, inside the created sheath is an area void of electrons. Injected electrons are exposed to the accelerating field and will continue to gain energy until they have reached dephasing.*

the laser pulse only positively charged ions are present. The concept is illustrated in Figure 4.1. The red ellipse at the right is the laser pulse, the gray lines the sheath electrons, and the black line illustrates the accelerating electric field gradient. E_z. In this picture, the electrons have been injected at back of the first wake directly after the laser pulse and are in an accelerating phase.

The laser pulse continuously excites a wake within the plasma, until the laser pulse energy is depleted; that is, until the energy loss is such that a nonlinear wave can no longer be excited. The sheath electrons are usually dense, and inside it, right behind the laser, a cavity with positively charged ions is created. The accelerating field E_z can attain a TV/m field gradient. In handy units, the field gradient is often given as $E_z \approx 96\sqrt{n_e[\mathrm{cm}^{-3}]}$ V/m. Thus, electrons injected to the structure can be accelerated to MeV energies over a distance of just a few millimeters. The maximum energy gain is determined by the distance over which electrons are exposed to the accelerating field. Due to the difference in the group velocity of the laser pulse and the speed of the electrons, $v_e > v_g$, the electrons will eventually outrun the laser. This is called dephasing, and is defined as the distance over which the electrons reach the midpoint of the plasma wave. At this position, the electrons see the negative potential at the front of the wave and the positive ions at the back, and will start to decelerate.

4.1.1 Ponderomotive force and wave excitation

One electron, exposed to an electromagnetic field, will experience a force according to the Lorentz force [26]:

$$\mathbf{F} = q(\mathbf{E} + \mathbf{v} \times \mathbf{B}), \tag{4.1}$$

where q represents the particle's charge, and hence for an electron, $q = -q_e$. In the case of nonrelativistic particles, only the electric field contribution is considered because the impact of a typical electromagnetic wave's magnetic field is much smaller than that of the electric field. However, because of the electron's low mass, it rapidly attains relativistic energies, and the magnetic contribution in eq. (4.1) can no longer be neglected. Moreover, the magnetic contribution leads to the nonlinear response of the electrons and to the ponderomotive force. This term will be the dominant one, as it increases with the increasing energy of the electron bunch.

LWFA relies on the excitation of waves in a non-linear manner, driven by the relativistic ponderomotive force which emerges when $a_0 > 1$, corresponding to laser pulse intensities exceeding 10^{18} W/cm^2 [4, 42]. For a typical gaseous target, the intensity at the edges of the laser pulse is sufficient to ionize it completely, leaving the central part of the pulse to interact solely with plasma. Electrons are displaced from regions of high intensity by the relativistic ponderomotive force and cannot recombine with their parent ions, creating a void in the path of the laser pulse. This resultant wakefield, or "bubble", as it is often called [10, 11, 44], is devoid of free electrons. When considering a laser pulse with an envelope that encompasses multiple cycles, the average relativistic ponderomotive force is described by [28, 42, 45]:

$$f_p = \frac{d\mathbf{P}_\perp}{dt} = -c^2 \nabla m_{\text{eff}} = -m_e c^2 \nabla \bar{\gamma} \tag{4.2}$$

where $\mathbf{P}_\perp$ is the transverse momentum of the electron and $m_{\text{eff}} = m_e\gamma$ is the relativistic mass of the electron. $\bar{\gamma}$ denotes the average Lorentz factor. On an ultra-fast timescale, specifically in the fs range, ions are stationary under the influence of the laser pulse. Eq. (4.2) does not consider a full cavitation behind the laser pulse, i.e., no bubble formation. In the nonlinear 3D regime, the ponderomotive force depends on the amplitude of the normalized vector potential, a_0. For $a_0 > 2$, a bubble is formed. Within the bubble, extreme electric fields (TV/m) are achieved, and electrons that escape the collective motion and become injected into the wave structure are accelerated to high energies.

4.2 The matched regime

Achieving energy breakthroughs in LWFA require electrons to remain within the accelerating structure, which led to the concept of the matched regime. This means that the laser pulse energy and duration have an optimum relationship, which in turn will lead to an optimum spot size so that a certain intensity can be reached. For this intensity, there is background plasma density that will lead to a self-guided laser pulse, so that an accelerating structure can be continuously excited throughout the whole length of the plasma.

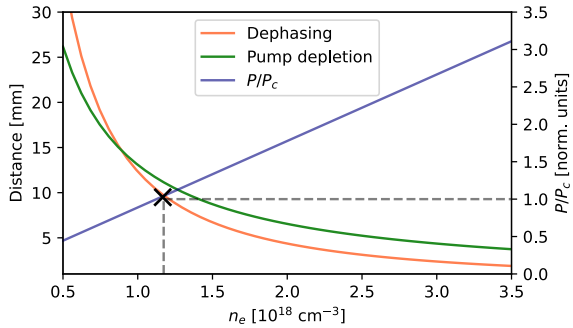

Figure 4.2. *The dephasing (orange) and the depletion of the laser pulse pump (green) as a function of the background plasma density, n_e. For both curves, the laser pulse has a center wavelength of 800 nm, a duration of 38 fs, and a pulse energy of 1 J. The assumed spot size is $W_0 \approx 10$ µm, leading to $a_0 = 2.5$,*

The self-guidance is achieved because of the radial change in the refractive index of the plasma, which is an effect of the excitation of a laser pulse with a radial distribution such as a Gaussian pulse. A Gaussian laser pulse can self-guide through the plasma beyond several Rayleigh lengths, and the change in refractive index is described by [46]:

$$n(\omega, n_\mathrm{e}) \approx 1 - \frac{1}{2}\frac{\omega_\mathrm{p}^2}{\omega^2}\left(1 + \frac{\Delta\eta}{n_\mathrm{e}}\frac{r^2}{W_0^2} + \frac{\Delta n_\mathrm{e}}{n_\mathrm{e}} - \frac{a_0^3}{8}\right), \tag{4.3}$$

In this context, Δn_e represents the reduction in density immediately following the laser pulse, caused by the ponderomotive force. The parameter $\Delta\eta = mc^2/(e^2\pi W_0)$ defines the density change required to minimize the oscillations of the laser spot size, W_0, ensuring that the laser pulse remains guided. The last term accounts for the relativistic electron mass change, as the laser pulse expels them. A laser pulse can self-guide if the refractive index change satisfies $\Delta\eta/n_\mathrm{e} \approx 4/(k_\mathrm{p}W_0)^2$, or if the mass correction satisfies $a_0/8 \gtrsim 4/(k_\mathrm{p}W_0)^2$ [46]. The last condition can be expressed in terms of the laser power, $P > P_\mathrm{c}$ [46, 47], where P_c is the critical power needed for self-focusing, defined by $P_c = 17\omega^2/\omega_\mathrm{p}^2$ [GW]. To achieve the bubble regime, it is necessary for the laser intensity to satisfy $a_0 > 2$, leading to the *matching* condition for the laser spot size (see eq. (2.11)):

$$a_0 \gtrsim 2\left(\frac{P}{P_\mathrm{c}}\right)^{1/3}. \tag{4.4}$$

Recall eq. (2.11), where $a_0 \propto \sqrt{I_0}$, which means that the intensity of the laser pulse must be such that the right-hand condition is fulfilled, which is obtained by focusing the laser pulse tightly. Since self-focusing

occurs when the fraction on the right-hand side is greater than one, the matched focal spot size is reached when $a_0 > 2$.

In Chapter 3, it was demonstrated that the phase velocity of an 800 nm laser pulse in plasma exceeds c. In contrast, the group velocity is slower than c due to plasma dispersion, causing the accelerating structure to move at $v_\mathrm{g} < c$. Electrons will rapidly reach $v_\mathrm{e} \approx c$, and since $v_\mathrm{e} > v_\mathrm{g}$, they will quickly enter a decelerating phase. This occurs over the dephasing length, which in the bubble regime is given by [46]:

$$L_\mathrm{d} = \frac{4\omega^2}{3\omega_\mathrm{p}^2}\frac{\sqrt{a_0}}{k_\mathrm{p}}. \tag{4.5}$$

In this domain, the plasma wave vector is given by $k_\mathrm{p} = \omega_\mathrm{p}/c$, where λ_w represents the nonlinear wake wavelength. As the laser pulse traverses the plasma, it modifies the refractive index, defined in eq. (4.3), requiring a time $t \approx 1/\omega_\mathrm{p}$ to efficiently guide the laser pulse. Consequently, the pulse's leading edge experiences diffraction. Insufficient guiding causes more of the laser pulse to diffract. Energy is also lost during wave excitation [47], with the plasma wave converting laser energy into the electron bunch. The pump depletion length [46] defines the maximum distance over which a laser pulse can generate a nonlinear wave:

$$L_\mathrm{pd} = \frac{\omega^2}{\omega_\mathrm{p}}\frac{\tau}{k_\mathrm{p}}, \tag{4.6}$$

where τ is the FWHM duration of the laser pulse. The dephasing length and pump depletion of eq. (4.5) and eq. (4.6) give the upper limit on the energy gain in the bubble regime. The plasma parameters, such as background electron density, are matched to the laser pulse intensity if $L_\mathrm{pd} = L_\mathrm{p}$. In this case, the laser energy is efficiently used to accelerate the electron bunch over the maximum distance before dephasing. This results in the following relationship between the laser pulse and plasma:

$$\frac{4}{3}\frac{\sqrt{a_0}}{\tau} = \left(\frac{n_\mathrm{e} q_\mathrm{e}^2}{\epsilon_0 m_\mathrm{e}}\right)^{1/2}. \tag{4.7}$$

This implies that specific laser pulses, matched in energy and time, correspond to an ideal plasma density for optimal acceleration. At this density, the plasma can efficiently balance the diffraction of the laser pulse, and the average electric field is $\bar{E} = m_\mathrm{e} c \omega_\mathrm{p} \sqrt{a_0}/(2q_\mathrm{e})$. Consequently, if the matched regime is reached, and the electrons are accelerated until dephasing and depletion are reached, the expected energy gain can be approximated by:

$$\Delta W \approx \frac{2}{3}\frac{\omega^2}{\omega_\mathrm{p}^2} m c^2 a_0. \tag{4.8}$$

Figure 4.2 illustrates the relationship between the dephasing length and the pump depletion with respect to the plasma density of a laser

pulse with $a_0 = 2.3$, a laser power of 26 TW, and $\tau = 38$ fs. The curves intersect at $n_e \approx 0.8 \times 10^{18}$ cm^{-3}, suggesting an optimal acceleration length of 15 mm. However, this density is insufficient to counteract laser pulse diffraction, as depicted by the blue line representing P/P_c. To efficiently guide the laser pulse under these conditions, external guiding is needed [46]. The gray dashed lines indicate the threshold plasma density needed for self-guidance of the pulse. Most experiments discussed in this thesis utilize $n_e \approx 3 \times 10^{18}$ cm^{-3}, which is ideal for effective self-guidance of the laser pulse. At these densities, the LWFA's limiting factor is the dephasing length, approximately 3.8 mm. However, during the experiment presented in this thesis, the acceleration length is approximately 1.5 mm, which leads to a theoretical maximum energy gain of $\Delta W \approx 200$ MeV.Under optimal experimental conditions, this is in good agreement with the observed energies, for example, achieved in Paper IV.

Table 4.1 summarizes typical experimental parameters for the LLC Ti:Sapphire and OPCPA systems, presenting actual experimental conditions in white and theoretically matched parameters in green with a star by the system name. For Ti:Sapphire, the laser pulse energy, a_0 and n_e, is kept unchanged for the matched calculations, which allows for calculations of the matched pulse duration and spot size. The maximum energy gain is then determined according to eq. (4.8). For the OPCPA system, the white row is based on current experimental conditions and with equations for the 1D linear regime presented in Lu et al. [46]. The maximum energy gain is obtained from the linear average field multiplied by the dephasing length. For the calculation of the matched parameters, the laser pulse energy and duration are kept constant to obtain matched W_0 and a_0. The spot size is made to fulfill $c\tau \lesssim W_0$. For the calculations presented in the table, self-focusing and self-compression, which increase a_0, are not taken into account [46, 48, 49]. These effects enhance maximum energy gain and injected charge. The influence of injected charge on the acceleration is also omitted, which alters the accelerating structure if the charge is substantial [50].

The table clearly shows that the OPCPA system is currently constrained by pump depletion in these experiments utilizing an unmatched spot size, while the Ti:Sapphire system is limited by dephasing. This fundamental distinction arises from the notably shorter pulse duration of the OPCPA system compared to the Ti:Sapphire system.

4.3 Injection methods

For the electrons to be exposed to high field gradients within the plasma, they must be injected into the accelerating structure. The terminology is adapted from acceleration physics, where the electron

Table 4.1. *Summary of the experimental conditions for the Ti:Sapphire and OPCPA systems in the white rows. The dephasing length, pump depletion, and energy gain are calculated on the basis of the measured energy, pulse duration, and laser spot size. The experimental energy gain is obtained by assuming that the maximum acceleration is limited by the laser pulse depletion. In the green rows, and marked with a star, are the matched conditions for each system. For the Ti:Sapphire system, the parameters are obtained by keeping a_0, $\mathcal{E}$, and n_e unchanged, while for the matched OPCPA, $\mathcal{E}$ and τ are the only constants.*

System	$\mathcal{E}$ [J]	τ [fs]	W_0 [μm]	a_0	n_e [10^{18} cm^{-3}]	L_d [mm]	L_{pd} [mm]	ΔW [MeV]
Ti:Sa	1.0	38	10	2.5	3	3.8	6.6	200
Ti:Sa *	1.0	22	6.6	2.5	3	3.8	3.8	510
OPCPA	0.22	9	19	1.3	8	2.8	0.19	70
OPCPA *	0.22	9	6	4.2	29	0.15	0.15	83

bunch is created outside the accelerating structure. For LWFA, the electrons are generated within the plasma itself, but the quality of the electron bunch is greatly influenced by how they are subjected to the accelerating gradient within the bubble. Traditionally, injection has been achieved using self-injection [6, 51]. Here, the laser amplitude is high enough for some electrons to break free from collective motion imposed by the ponderomotive force, disrupting the wave structure. This injection method is sensitive to plasma and laser pulse fluctuations, which cause significant fluctuations in the energy and charge of the accelerated bunch. Therefore, tremendous work on injection control has been done over the last decades.

The electrons can be trapped within the wake if their initial velocity is close to the velocity of the wake, that is $\gamma/\gamma_\mathrm{p} \approx 1$, where γ_p is the Lorentz factor of the plasma wave. All other electrons contribute to the background plasma. The different initial conditions of the electrons subsequently lead to different trapping positions and times. If the electrons are trapped at different positions and times, they acquire different final energies, essentially leading to a wide energy spread. The derived matched parameters provide a foundation for optimizing the acceleration process. However, laser parameters are often predefined, meaning that, unless the laser is specifically designed for the LWFA experiment, it is typically unmatched. To overcome this and enhance control over the acceleration, various injection and acceleration strategies using plasma tailoring have been developed. Discussed here are the ionization injection scheme and the shock-front injection.

4.3.1 Ionization injection

A prevalent and simple injection method is the ionization injection scheme [52–54]. The host gas used is typically a low Z-number gas, such as molecular hydrogen or helium, doped with a higher Z-number

gas. Interestingly, at intensities near 10^{19} W/cm^2, molecular nitrogen proves to be an ideal option.

Table 4.2. *The appearance intensity of helium and nitrogen, for each ionization stage. The two innermost K-shell electrons of N are marked in green.*

Z_i	He [W/cm^2]	N [W/cm^2]
1^+	1.5×10^{15}	1.8×10^{14}
2^+	8.8×10^{15}	7.7×10^{14}
3^+		2.3×10^{15}
4^+		9.0×10^{15}
5^+		1.5×10^{16}
6^+		1.0×10^{19}
7^+		1.6×10^{19}

In the outer regions of the laser pulse, nitrogen reaches its fifth ionization state at intensities of 10^{16} W/cm^2. These electrons contribute to the background plasma density for LWFA. As the laser pulse's peak intensity moves through plasma, it can also ionize K-shell electrons. By then, a plasma cavity exists and the trapping condition is therefore relaxed since electrons are close to the peak intensity. Electrons located close to the wake are exposed to the wake potential and can be trapped. The electrons on the axis have the largest change in wake potential and are easily trapped, while off-axis electrons, away from the wake, contribute to the background density [53]. Since the electrons are injected as long as the laser pulse intensity is enough to drive a wake and ionize the K-shell electrons, this scheme relaxes the demands on the laser pulse needed for efficient trapping. Table 4.2 lists the field ionization intensities for nitrogen and helium, defined by the appearance intensity [28], which is the intensity seen by the bound electron:

$$I_{\mathrm{app}} = \frac{cI_{\mathrm{p}}\pi^2\epsilon_0^3}{2Z_{\mathrm{i}}q_{\mathrm{e}}^6}, \tag{4.9}$$

where I_{p} represents the ionization potential of the ion and Z_{i} denotes the charge of the resulting ion. Electron injection in this setup is experimentally straightforward due to the relaxed LWFA matching conditions. However, as the laser pulse undergoes self-focusing, self-compression, and self-guiding in the plasma, it sustains the intensity needed to ionize nitrogen's K-shell electrons throughout gas propagation, resulting in a 100% energy spread in the electron spectrum. This technique is used in Paper VI to produce stable high-flux x-rays. Moreover, the length of the gas cell exceeded the length of the dephasing, enhancing the generation of x-rays [55].

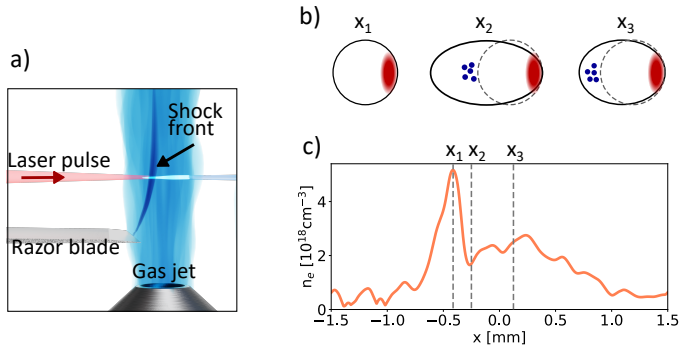

Figure 4.3. *Shock-front injection concept. a) Diagram of a supersonic gas jet. A razor blade disrupts the gas flow, creating an upstream shock-front. b) A laser pulse propagates from left to right through the gas. The plasma wavelength varies along the jet, as* $r_b \approx \lambda_w \propto \sqrt{n_e}$*. Each point in b) aligns with the highlighted positions in c) which display an experimentally derived plasma density profile.*

4.3.2 Shock-front injection

Shock-front injection is a method to reduce the energy spread of electron bunches [56–62]. It involves disturbing a supersonic gas flow by placing a sharp object, such as a razor blade, near the gas flow boundary, as depicted in Fig. 4.3a). At supersonic speeds, gas molecules predominantly continue their supersonic course when encountering the object [63]. This creates a denser gas region upstream of the flow, resulting in a dense electron region at the jet's start. As the laser pulse passes through, the excited bubble will change because of its dependence on the plasma density, $r_\mathrm{b} \approx \lambda_\mathrm{p} \propto \sqrt{n_\mathrm{e}}$. The bubble initially contracts and then expands rapidly in the high-to-low-density transition (Figures 4.3b) and c), from x_1 to x_2), injecting the former rear electrons into the accelerating structure [64–70]. At the shock-plateau junction (x_2 to x_3), the bubble contracts again, mitigating further injection. The brief duration of this event allows for concurrent electron injection, forming a quasi-monoenergetic bunch. Despite being sensitive to laser parameters and having a limited injection capacity, this technique is adaptable to various geometries and offers a robust approach to plasma control.

4.3.3 Shock-assisted ionization injection

A method that harnesses the benefits of both ionization injection and shock front injection is the so-called shock-assisted ionization injection [58, 59]. In Paper I, this method is used to generate stable quasi-monoenergetic electron bunches. The host gas is helium and the dopant is 1% nitrogen. Figure 4.4 presents typical experimental results of

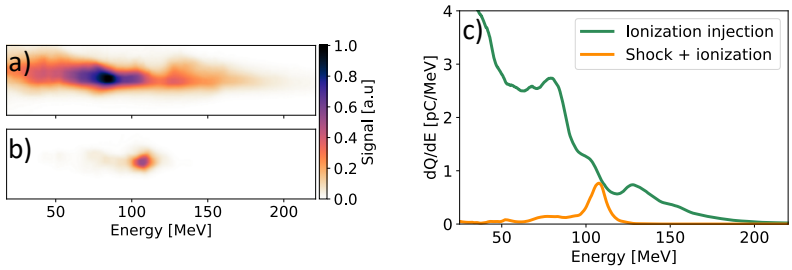

Figure 4.4. *A demonstration of the difference in the electron spectrum with a) ionization injection and b) shock-assisted ionization injection. In c), the integrated spectrum of a) is shown in green and b) in orange.*

the ionization injection and shock-assisted ionization injection method. In Figure 4.4 a), ionization injection results in a notable energy spread. The mechanism produces stable electron bunches in terms of charge and energy, but the spread in energy is 100%. Figure 4.4 b) displays a quasi-monoenergetic spectrum due to the introduction of the shock front. Figure 4.4 c) integrates the two spectra, clearly showing the difference in the injected charge and energy characteristics.

In contrast to shock-assisted injection in a single gas like helium, in this context, injection is initiated by both the density gradient and the laser pulse's self-focusing, combined with the ionization which relaxes the trapping condition. After the shock, as depicted in Figure 4.3, the bubble expands between x_1 and x_2, and laser diffraction reduces a_0 below the intensity necessary to ionize the K-shell electrons of nitrogen. The combination of several injection techniques leads to a stable injection of high-quality electron bunches. In this thesis, it is the most successful technique for stable generation of quasi-monoenergetic electron bunches.

As the blade can be moved across the gas jet orifice, the length of the plateau can be adjusted. The energy gain of an accelerated particle can be expressed as $\Delta W = \bar{E}_\mathrm{l} L$, where $\bar{E}_\mathrm{l}$ is the average electric field gradient and L the acceleration distance. This relationship was used in Paper I to determine $\bar{E}_\mathrm{l}$, based on the measured energy ΔW and the recorded plateau length, L.

4.4 Betatron radiation

In the bubble regime of LWFA, the radial force that pushes the electrons toward the optical axis causes them to oscillate around the it [71–74]. The oscillation causes the electrons to emit radiation and, since they are highly relativistic, this radiation lies within the x-ray spectral domain and has a synchrotron-like spectrum. These betatron oscillations give the radiation its name. Since they are of similar duration as the laser

pulse, in the fs regime, they are an important addition to conventional x-ray sources, where the fs domain is challenging to reach. Due to the small source size, defined by the wakefield size, which is on the order of magnitude of the focal spot size, betatron radiation allows for high-resolution imaging.

By realizing that the betatron oscillation resembles that of an undulator, well-established physics can be adapted to x-rays generated in the bubble regime, as described below. The radiation occurs from the transverse motion of the electron within the bubble. Thus, the transverse equation of motion within the bubble that describes this oscillation for one electron is [75]:

$$\frac{d\mathbf{P}}{dt} = -m_\mathrm{e}\omega_\mathrm{p}^2\mathbf{r}_\perp/2 + m_\mathrm{e}c\omega_\mathrm{p}\mathbf{u}_\mathrm{z}. \tag{4.10}$$

Note that the equation of motion differs from eq. (4.2), because of the absence of the electromagnetic field from the laser pulse. $\mathbf{r}_\perp$ is the radial position and $\mathbf{u}_\mathrm{z}$ is the unit vector in the direction of the wakefield propagation; that is, in the direction of the laser propagation. For small oscillation amplitudes, the fundamental frequency of the betatron motion can be defined as:

$$\omega_\beta = \omega_\mathrm{p}/\sqrt{2\gamma}. \tag{4.11}$$

As noted, the relativistic energies of the electrons lead to a synchrotron-like spectrum being emitted, with a fundamental wavelength of:

$$\lambda = \lambda_\beta/2\gamma^2, \tag{4.12}$$

where λ_β is the period of the betatron oscillation, analogous to the magnet period in an undulator. The radiation is emitted mainly in the forward direction and the cone of emission, which coincides with the oscillation angle, also defined as the divergence of the radiation depends on the oscillatory strength parameter, K by:

$$\theta \simeq K/\gamma. \tag{4.13}$$

K is usually termed the strength parameter. For large oscillation amplitudes, which is:

$$K = 1.33 \times 10^{-10}\sqrt{\gamma n_\mathrm{e}[\mathrm{cm}^{-3}]}r[\mu\mathrm{m}]. \tag{4.14}$$

In this context, r describes the oscillation radius. The divergence in eq. 4.13 increases with increased strength K but decreases at higher particle energies, due to the force required for high-energy particle deflection. Since the bubble is small and increases with increasing density $\lambda_w \propto 1/\sqrt{n_\mathrm{e}}$, the ion cavity within which the electrons can oscillate is small, which also leads to K and subsequently θ being

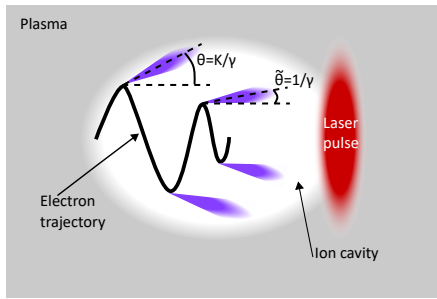

Figure 4.5. *A schematic illustration of the betatron radiation. The laser pulse propagates from right to left in the figure.*

large [43, 76–78]. Consequently, along with eq. 4.11, the spectrum exhibits angular dependence. The typical peak particle energy in these experiments, with $\gamma \approx 300$, results in an rms divergence of about 10-15 mrad when used in eq. 4.14 and eq. 4.13.

The radiated synchrotron spectrum is described by:

$$\frac{dI}{d\omega} = \frac{1}{4\pi\epsilon_0}\left(\frac{3\pi}{c}\right)^{1/2}\frac{q_e^2}{c}\gamma\frac{\omega}{\omega_c}\int_{\omega/\omega_c}^{\infty} K_{5/3}(x)dx, \tag{4.15}$$

where $K_{5/3}$ is the modified Bessel function. In this context, ω refers to the x-ray frequencies generated. The spectral intensity rises to the crest and then decreases exponentially with photon energy. The critical frequency, ω_c, defines the characteristic spectrum:

$$\omega_c = \frac{3}{2}\frac{\gamma^3\omega_\beta^2 r}{c}. \tag{4.16}$$

Thus, with a smaller oscillation radius, r, the critical frequency increases. The above expressions indicate that the critical frequency increases with the cube of the electron's energy, γ^3. Clearly, the properties of the electron bunch affect the x-ray characteristics. In the ionization injection method, a short overlap occurs between the electron bunch and the laser pulse, causing electrons to be "kicked" along the laser's polarization direction (importantly, this interaction is not caused by the ponderomotive force). This will cause an elongation of the x-ray beam profile, which coincides with the polarization of the laser pulse [79, 80]. Conversely, when a significant overlap occurs between the laser pulse and electrons, it can enhance oscillations, thereby increasing the x-ray flux. Unlike the optimized LWFA for electron quality, where electrons accelerate only until dephasing is reached [46], surpassing this point may be beneficial for optimizing x-ray flux [55, 81]. Different optimizations, similar to those used for electron bunches, can be assessed, focusing on achieving the highest critical energy or maximum x-ray flux. The electron energy significantly influences the critical energy; thus, raising

electron energy yields harder x-rays. Conversely, x-ray flux benefits more from a larger number of radiating electrons, often resulting in an LWFA functioning at an electron density higher than that which produces highly energetic electron bunches. A multijet scheme has been shown to improve the flux of X-ray photons and the critical energy as well [82], but similarly to an increased background plasma density, the transverse size of the electron bunch increases. However, such a scheme shows the level of versatility that an LWFA source has.

4.4.1 X-ray detection and spectrum determination

X-rays can be detected directly, or indirectly, where indirect detection techniques involve a radiochromatic medium. Direct x-ray detection frequently employs a deep-depletion CCD chip, where the x-rays impinging on the chip cause a cloud of electrons to be released, which is converted to a signal count. The number of released electrons is proportional to the number of detected photons and their energy. A higher photon energy thus gives rise to a larger electron cloud. The CCD chip thus serves dual purposes: precise x-ray imaging and as an x-ray spectrometer. The imaging process is straightforward, as varying degrees of x-ray transparency in materials and objects create shadowgraphic images.

A common technique for spectrum determination is the Ross filter system [83, 84]. The method determines the spectrum using imaging of metal foils utilizing their different K-edge absorption properties. The technique requires an initial assumption of the spectral shape, which is fitted to the experimental data. The critical energy, or frequency, is obtained by using a filter array, which in this case are the metal foils. This approach is suitable for a polychromatic source, such as the one discussed here. A filter array is placed before the detector, allowing the measurement of the total transmission through each filter, as illustrated in Figure 4.6 a). The average transmission of each filter site is shown in Figure 4.6b). Spectrum reconstruction assumes that the normalized emitted on-axis spectrum is as follows:

$$N(E) = \left(\frac{1}{2}\xi K_{2/3}(\xi/2)\right)^2 \tag{4.17}$$

with $\xi = E/E_\mathrm{c}$, and where $E_\mathrm{c} = \hbar\omega_\mathrm{c}$ is the critical energy. $K_{2/3}$ is the modified Bessel function. By assuming this spectral shape, for a range of critical energies, the actual critical energy can be found by the least-squares method:

$$\Lambda^2(E_\mathrm{c}) = \sum_\mathrm{i} (\tilde{T}_{\mathrm{i},E_\mathrm{c}} - \hat{T}_\mathrm{i})^2, \tag{4.18}$$

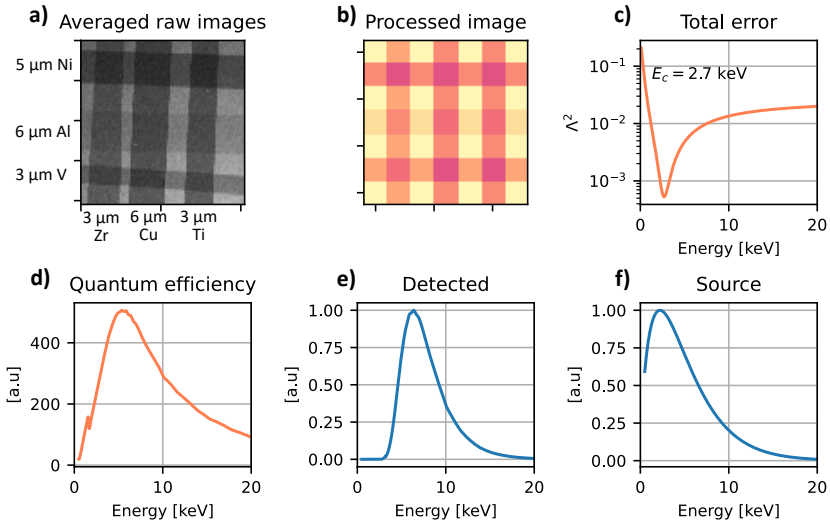

Figure 4.6. *Determination of the x-ray spectrum using a Ross filter array: a) displays an average of 10 raw images, with dark areas indicating foil positions. Overlapping filters create more transmission curves for spectrum determination. Each filter site is averaged, shown in b). c) presents the error curve from the least-squares method described in eq. (4.18). In d), the camera's quantum efficiency is plotted to indicate the spectral response of the CCD chip. e) presents the reconstructed recorded spectrum, while f) shows the reconstructed source spectrum.*

where $\tilde{T}_{\mathrm{i},E_\mathrm{c}}$ is the theoretical transmission of a spectrum with critical energy E_c through the foil i, and $\hat{T}_\mathrm{i}$ is the measured transmission through foil i. The transmission curves for each foil are obtained from listed database values [85]. E_c is found where Λ^2 assumes its minimum value, depicted in Figure 4.6 c). With the E_c found by eq. (4.18), the normalized theoretical total transmission through any filter array can be determined by:

$$\tilde{T}_{\mathrm{i},E_\mathrm{c}} = \frac{\int_0^\infty N(E) Q_\mathrm{E} T_\mathrm{t} T_\mathrm{i} dE}{\int_0^\infty N(E) Q_\mathrm{E} T_\mathrm{t} dE}. \tag{4.19}$$

Here, T_i represents the transmission through filter i, Q_E is the quantum efficiency of the camera, and T_t is the overall transmission without the filter array. The Andor iKon-L SO back-illuminated deep-depletion CCD [86], exhibits an optimal response near 5 keV, as illustrated in Figure 4.6 d). Figures 4.6 e) and f) depict the reconstructed detected spectrum and the estimated source spectrum, respectively. This method was applied in Paper VI to identify the x-ray spectrum used to calculate the liquid volume fraction.

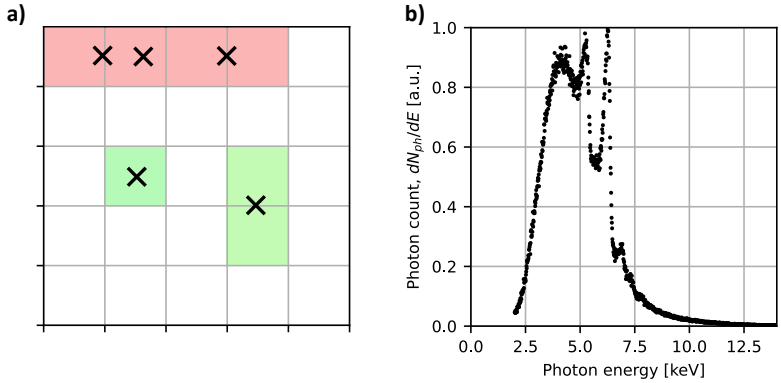

Figure 4.7. *The principle of SPC in a), where each square represents a pixel. The crosses symbolize x-ray photons. The red pixels represent events where it is not possible to distinguish a single photon, while green pixels are accepted as single-photon events. b) shows an experimentally recorded spectrum.*

Paper IV uses single photon counting (SPC) [87] for spectrum determination. This method takes advantage of the characteristics of the CCD. Each x-ray photon generates an electron cloud within the chip. The electron count in the cloud is influenced by the photon energy and the chip's quantum efficiency. Pixel groups unidentifiable as single-photon events are dismissed, whereas identifiable single-pixel or cluster events are recorded. Figure 4.7 a) demonstrates the concept using a 5×5 pixel matrix, and Figure 4.7 b) depicts the resulting spectrum. In the SPC spectrum, fluorescence peaks from vacuum-chamber materials are observed, because the SPC directly measures the spectrum, unlike the Ross filter array, which is an indirect measurement method. This does not imply that these peaks are missed with the Ross-filter array; rather, they are excluded from the reconstructed spectrum.

Both the Ross filter method and the SPC are powerful methods for the spectrum detection of x-rays generated through LWFA. To apply the Ross filter detection, an initial source shape must be assumed. Because of the characteristics of the electron source, a synchrotron-like spectrum is a valid guess. The number of filters used for spectrum detection also influences the accuracy of the method. In this thesis, the technique has been applied assuming no angular frequency dependence, but if the filter thickness and position relative to the source are chosen carefully, it is possible to retrieve this as well. The SPC technique requires single-photon events and is usually ensured by positioning the camera far away from the source, so the divergence of the x-ray beam ensures that each photon is spatially separated on the chip. The initial source shape is therefore not taken into account. The angular spectral dependence is thus also omitted. However, this technique captures the true spectrum

at the central part of the beam, without making any initial guesses at the spectral shape. Therefore, the two techniques presented complement each other.

4.5 Applications

Due to their short pulse durations, high brightness, and high resolution provided by the small source size, LWFA-generated x-rays have a wide range of applications and are well suited for x-ray tomography. As described in Paper VI, these x-rays serve as an alternative to synchrotron sources for imaging things like atomizing sprays. Previous research by our group has already demonstrated the practicality of these applications [88, 89]. Unlike earlier studies, Paper VI presents time-resolved measurements, which illustrate how the mass distribution changes within the spray plume. The spray nozzle was mounted on a rotational stage to capture a full 360° perspective, allowing spray reconstruction similar to the density determination outlined in Chapter 3, thus allowing estimation of crucial metrics such as the liquid volume fraction.

4.5.1 Tomographic reconstruction

A common technique for 3D reconstruction of 2D images is inverse back projection [90]. Similarly to the Abel inversion, the forward transform projects a 3D object in a 2D space, and the inverse transform does the opposite. For the filtered back projection technique, no rotation-symmetry assumption is needed. However, the object of interest must be sampled at enough angles to avoid image artifacts. In x-ray tomography, the attenuation coefficient is reconstructed. The Beer-Lambert law describes exponential attenuation through any medium:

$$N = N_0 e^{(-\int_r \mu(x,y_1))dx}. \tag{4.20}$$

The detected signal N will be some fraction of the source signal N_0. The attenuation coefficient $\mu(x, y_1)$ is a combination of absorption and scattering. For most materials and x-ray energies [90],

$$\mu = \rho \left[a \frac{Z^{3.8}}{E^{3.2}} + b \right] \tag{4.21}$$

where E is the x-ray energy, Z is the atomic number, and ρ is the mass density. The first portion of the equation represents the photoelectric absorption and the second Compton scattering, with associated constants a and b.

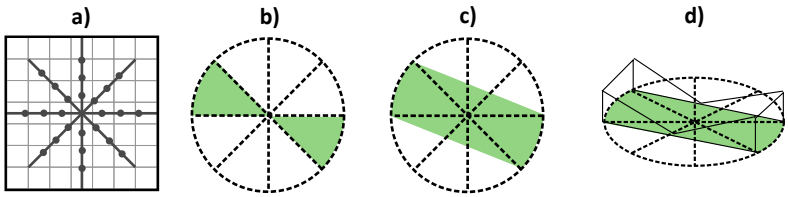

Figure 4.8. *Illustration of the projection data in the real space, a) and representation in Fourier space, b) - d). In a), the lines combined with the dots represent the sampling data, and the grid represents the Cartesian space. The shaded green area in b) depicts the ideal Fourier space data, while the shaded green area in c) is the actual Fourier space obtained from the projection data in a). The wedge in d) represents the weight function $|\omega|$, used to approximate the ideal sampling in b).*

The sampling of an object at different angles results in the full 2D Fourier transform, by the Fourier slice theorem [90]. The filtered back projection of the 2D projections, $p(t, \theta)$, is given by:

$$f(x,y) \int_0^{\pi} \int_{-\infty}^{\infty} P(\omega,\theta)|\omega| e^{i2\pi\omega(x\cos\theta + y\sin\theta)} d\omega d\theta \tag{4.22}$$

where $P(\omega, \theta)|\omega|$ together with the integral of ω represents the Fourier transform of $p(t, \theta)$. $|\omega|$ is a weight function, illustrated in Figure 4.8. This weight is included to account for the undersampling of higher spatial frequencies, which occur due to the cylindrical sampling of the Cartesian coordinate system. Figure 4.8 a) illustrates the projection data, while Figures 4.8 b)-d) illustrate the different filters in Fourier space. Ideally, the Fourier space projection would have the shape illustrated by the green-shaded area in b), as this would result in an aberration-free reconstruction. The actual data are represented by the green-shaded area in c). The weight function $|\omega|$ is usually formulated as a wedge in d), which approximates the ideal sampling shown in b).

4.5.2 Experimental setup and results

In Paper VI, the 2D x-ray absorption images are recorded in line of sight. The spray nozzle is mounted on a rotating stage, allowing the spray to be recorded from several angles, as illustrated in Figure 4.9. The number of projection angles needed is determined by the sampling theorem, which in general is $N = N_{pixels}\pi/2$, where N_{pixels} is the number of pixels on the camera chip used to record [90]. In the paper presented, the sampling theorem is not fulfilled, which can lead to image artifacts, such as strikes across the reconstructed 3D image. This was partly solved by making use of the spray's rotation symmetry, meaning that a full 360° recording is not needed to capture all features of the spray. However, some striking artifacts are present, as seen in the 2D slices of Figure 4.9.

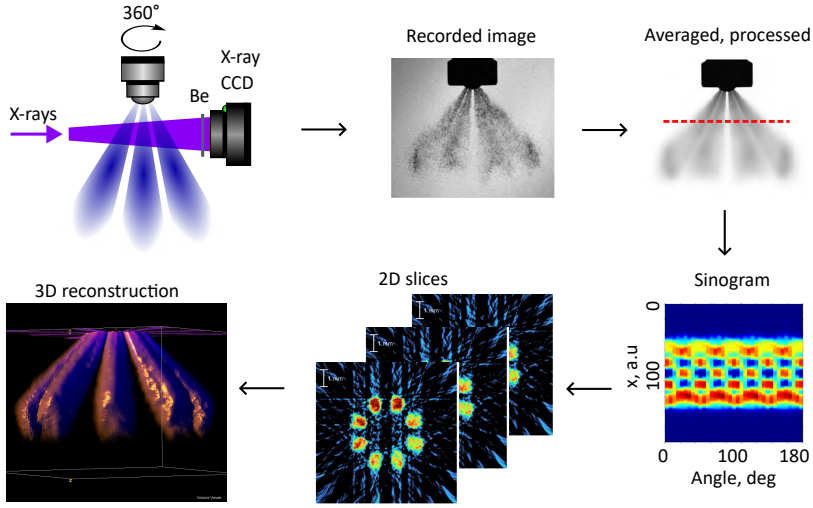

Figure 4.9. *The process of the tomographic reconstruction. The images are recorded in line of sight, where the spray and camera are positioned in air outside the vacuum chamber. The spray can rotate 360° to capture several projection angles. In the recorded single-shot image, the individual droplets are clearly visible. The background is not homogeneous, which must be corrected. To increase S/N, 10 images are averaged. The sinogram is obtained at one height slice, shown in the processed image by the dashed red line, for all different angles. From the sinogram, the 2D slice can be reconstructed at a certain height. The full 3D image is obtained by adding the slices together. Image 4-6 courtesy of Erik Löfquist.*

Figure 4.9 illustrates the experimental setup outside the vacuum. The spray is mounted on a rotating stage to capture various projection angles while keeping the x-rays and camera fixed. The second image shows an example image where individual droplets in the spray are sharply defined. To enhance S/N, 10 images from the same angle are recorded, and background radiation is flattened, leading to a processed average image. In one specific slice, marked by red dashed lines across all angles, the sinogram in the fourth image is extracted. This represents a 2D intensity projection. Using the filtered back projection method, as described in eq. (4.22), 2D slices are generated at each height. Adding these height slices reconstructs the complete 3D image. To retrieve physical information, such as the liquid volume fraction, the x-ray source must be fully characterized. In the presented experiment, this is done using the Ross Filter method described in the previous section. The liquid volume fraction is obtained from the 2D slices alone, revealing crucial nozzle features such as spray efficiency.

Chapter summary

This chapter outlines the fundamental concept of LWFA, highlighting electron acceleration and x-ray emission. It reviews various injection methods, focusing on the ionization injection scheme and the shock-assisted ionization injection scheme, both of which are the most robust discussed here. The chapter concludes with an explanation of betatron radiation and its practical uses. The next chapter delves into radiation control.

Chapter 5

Beam control

This chapter covers the principles of the results presented in this thesis, in particular Papers I, II, IV and V. On of the key findings of this thesis discussed in Papers II and IV, is the emission of low divergence x-rays that approaches the incoherent limit. Beam control becomes important in applications and staging between several accelerator stages. The chapter is divided into three main parts. The first part covers the usage of plasma lenses, the second how a similar setup can be used to overcome the dephasing length of LWFA, and lastly the beam-pointing dependence on the laser pulse spatiotemporal couplings is discussed.

5.1 Plasma lenses

Electron bunches generated by LWFA often exhibit significant divergence due to the strength of the focusing fields in the compact accelerating structure, restricting their practical applications. Quadrupole magnets can focus these electron bunches and have been shown to be useful in Ti:Sapphire-driven LWFA, which is the focus of this thesis [91]. However, quadrupoles need a bunch that is monochromatic and stable pointing. A plasma lens (PL) is an alternative approach to manipulate the LWFA electron bunch [23, 92, 93], offering high magnetic and radially symmetric fields to focus highly relativistic electrons. PLs can be used actively [94, 95] or passively [23, 93, 96–98]. In active PLs, a discharge current in a capillary tube induces symmetric azimuthal magnetic fieldsincrease with the capillary radius.

In the passive PL, the electron bunch from the initial acceleration activates the focusing magnetic field. Passive lenses are advantageous because of their robustness against pointing variations of the incoming electron bunch and their natural achromatic properties. Similarly to the LWFA plasma regimes, the PL can be operated in the underdense

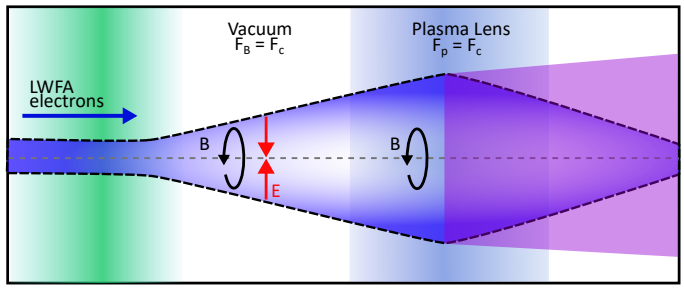

Figure 5.1. *The envelope of the electron bunch as it propagates from vacuum to the plasma lens. In vacuum, the electric field E that leads to the force due to the space charge, F_c, and the self-generated magnetic field B that leads to the radial force, F_B, are of equal magnitude and balance. Within the PL the group of electrons causes a shift in plasma electrons, which leads to a force F_p, equal to and opposite to F_c. The remaining force is thus F_B. The deflection within the lens leads to x-ray emission, illustrated in purple.*

[23, 93, 96–98] or overdense regime, both of which are defined with respect to the electron bunch density, n_b [92, 99]. The lens is in the underdense regime if $2n_\mathrm{b} > n_\mathrm{e}$ [92]. In this scenario, the electron bunch's leading edge possesses a sufficiently high current to generate a nonlinear plasma wave within the PL, effectively focusing the trailing electrons. Therefore, the focal length is influenced by the wake excitation, which in turn is affected by the PL's background plasma density. This regime is interesting because it is also employed in multistage LWFA – particle wakefield acceleration (PWFA) [99–102]. In the particle-driven regime, dephasing does not impact the acceleration process, as both the driving and accelerated electrons travel at the same speed.

In the overdense regime, where $n_\mathrm{b} < n_\mathrm{e}$, the electron bunch causes a displacement of plasma electrons, leading to a force acting on the bunch of the order of magnitude of the space charge. The focus result depends on the density of the bunch. Due to the high-density plasma, the response time of it ω_p is too fast compared to the bunch length, preventing coherent wake formation, rendering this regime unsuitable for acceleration. Nevertheless, this scenario merits attention for electron bunch energy and x-ray generation. For a very dense PL, the electrons will emit low-divergence x-rays. Interestingly, a nearly identical PL configuration can function as a rephasing stage, overcoming the LWFA energy gain limit.

5.1.1 The overdense laser plasma lens

The electrons within an electron bunch traveling in free space will naturally maintain their trajectory as the forces from the radial electric field **E** and the self-induced magnetic field **B** balance. Figure 5.1

illustrates the effect, where the blue region outlined by the dashed black line represents the enevelope of the electron bunch as it propagates from the LWFA to the PL. F_{c} denotes the space charge, induced by $\mathbf{E}$, and F_{B} the force of $\mathbf{B}$, described in more detail in the following. Upon entering the overdense plasma, the displacement of plasma electrons will apply a force equal to and opposite to the bunch space charge, denoted F_{P}, as shown in Figure 5.1 b). The remaining force from the self-generated magnetic field will pinch the electron bunch, creating a focusing effect. According to Ampère's law, the magnetic field $\mathbf{B}$ generated by a current density $\mathbf{J}$ across a surface is equal to the enclosed current I within an Ampèrian loop [26].

$$\oint_C \mathbf{B} \cdot d\mathbf{l} = \mu_0 \int \mathbf{J} \cdot d\mathbf{a} = \mu_0 I. \tag{5.1}$$

For an electron bunch, the current density J can be expressed in terms of the electron bunch density as $J = q n_{\mathrm{b}} v_e$. For a uniform bunch, (for example, a cylinder with radius r) $J = n_{\mathrm{b}} e \pi r^2$, the azimuthal magnetic field for an electron bunch propagating at a speed that approaches the speed of light in vacuum $v_e \approx c$ is:

$$B_\theta = n_{\mathrm{b}} q_e \sqrt{\frac{\mu_0}{4\epsilon_0}} r. \tag{5.2}$$

From the Lorentz force in eq. (4.1), the radial force acting on the highly relativistic electron bunch is given solely by the magnetic contribution. In this case, the radial force can be approximated as:

$$F_{\mathrm{r}} \approx q(\mathbf{v} \times \mathbf{B}) = -q_e(cB_\theta). \tag{5.3}$$

Inserting eq. (5.2) into eq. (5.3) leads to the following expression of the radial force:

$$F_{\mathrm{r}} = -\frac{q_{\mathrm{e}}^2 n_{\mathrm{b}}}{2\epsilon_0} r. \tag{5.4}$$

From eq. (5.4), the force must be directed in the negative radial coordinate, resulting in a radial focusing force. It is also symmetric around the propagation axis and increases with increasing bunch density. This type of linear force profile ensures that all electrons experience a force proportional to their radial displacement, preventing emittance growth. Similarly to an optical lens, the particles the furthest away from the axis will experience the strongest force, deflecting them towards the propagation axis, z.

For a non-uniform density distribution, such as a Gaussian bunch, with a radial charge distribution such that the current density is $\mathbf{J} = q n_{\mathrm{b}} c \exp(-r^2/2\sigma_{\mathrm{r}}^2 - z^2/2\sigma_z^2)$, where σ_{r} denotes the radial rms size, the magnetic field after the Ampère's law has been applied reads:

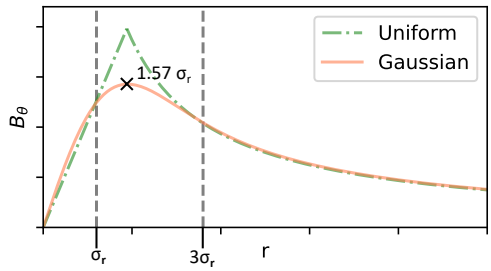

Figure 5.2. *A comparison of the magnetic field generated from a uniform bunch (green) and a Gaussian bunch (orange). The cross in the figure shows the radial position where the magnetic fields attain the maximum value,* $1.57\sigma_r$*. In the figure, the two gray dashed lines mark the radial positions for* σ_r *and* $3\sigma_r$*.*

$$B_\theta(r,z) = \frac{\mu_0 q_e e c n_b \sigma_r^2}{r}\left(1 - e^{-r^2/2\sigma_r^2}\right) e^{-z^2/2\sigma_z^2}. \tag{5.5}$$

Unlike eq. (5.2), the generated magnetic field varies in time as well, imposed by the longitudinal distribution in z. In Figure 5.2 b), eq. (5.2) and (5.5) are plotted for different r with $z = 0$. In green is the magnetic field of the uniform distribution, eq. (5.2) for a bunch radius $r = 1.57\sigma_r$, coinciding with the maximum field of the Gaussian bunch. σ_r denotes the rms deviation of a Gaussian electron bunch in this example. Outside the bunch, for $r > 1.57\sigma_r$, the magnetic field strength decreases as $B_\theta \propto 1/r$. The orange line shows eq. (5.5). The magnetic field reaches its maximum value at $r = 1.57\sigma_r$, and then decreases exponentially. At $r = 3\sigma_r$, the magnetic field strength has dropped by about 30% of the maximum value. Both curves are plotted with the assumption of a bunch with the same density but different charge distributions. The maximum magnetic field strength induced by an electron bunch with a Gaussian distribution, and with $z = 0$ can now be expressed in terms of the bunch charge.

$$B_\theta^{max} \approx \frac{0.45\mu_0 c Q}{(2\pi)^{3/2}\sigma_r\sigma_z}. \tag{5.6}$$

Assume a bunch with $Q = 200$ pC, radial rms $\sigma_r = 5$ µm and a longitudinal size of $\sigma_z = 5$ µm, the maximum magnetic field becomes $B_\theta^{max} \approx 85$ T. The next section will discuss the consequences of this magnetic field in terms of x-ray radiation. To no surprise, this field quickly grows large with reduced bunch size, which is still in agreement with the initial definition of the overdense plasma lens dependence on the bunch density.

The PL is experimentally realized by adding another supersonic gas jet downstream of the first jet, where the LWFA occurs, as depicted in

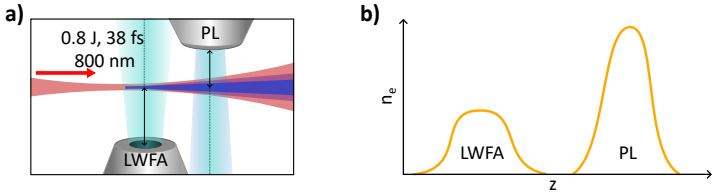

Figure 5.3. *Schematics of the plasma lens setup and the approximate density profile. In a), the laser pulse (red) enters from left and is focused at the beginning of the orifice to the jet where LWFA occur. The laser pulse, with electron bunch (blue) and x-rays (purple), co-propagate to the second jet, marked PL. In b) a sketch of the density profile from this setup is provided.*

Figure 5.3 a). Each jet is marked with its functionality. Figure 5.3 b) shows two illustrative density profiles from the setup in a). The plasma lens described in Paper I focuses quasi-monoenergetic electron bunches, achieving a 40% reduction in transverse size under optimal conditions , from approximately 6.5 mrad FWHM to approximately 4 mrad FWHM. As LWFA technology progresses, in terms of stability and beam quality, these electron bunches are increasingly suitable for FELs [24, 103, 104]. This setup demands electron bunches with minimal energy spread, limited divergence, and low emittance. The LWFA-PL approach displays strong potential for use as a fully LWFA FEL seeder and is promising for multistage acceleration, targeting unprecedented particle energies [99, 101], which in turn will enable new research areas. As discussed in Chapter 4, the deflection of the electron bunch causes emission of x-rays. These x-rays are emitted around the crest of the oscillation, where the acceleration is the largest.

5.1.2 Low-divergence x-ray radiation

Several studies of decoupled LWFA and PL processes focus on enhanced x-ray radiation, particularly focusing on critical energy and photon flux [105, 106]. These studies employ PLs with a plasma density greater than that of the LWFA jet, yet it remains below overdense levels. As a result, the enhanced radiation dynamics is influenced by wake excitation in the second density region, initiated either by the drive laser or the electron bunch. The pinching effect of the bubble in an upramp also contributes to increased x-ray radiation following a similar principle [107]. This section aims to explore the behavior of x-ray radiation within the overdense regime. In the mentioned configurations, the x-ray beam profiles remain unchanged compared to a single LWFA scheme. With the x-ray beam's significant divergence, approximately 20 mrad in this thesis, its applications are limited. However, some applications take advantage of this divergence to facilitate magnified imaging of small objects and

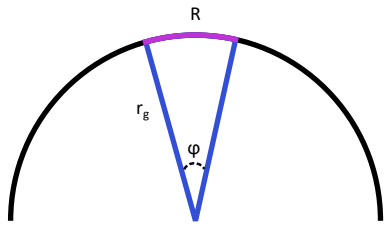

Figure 5.4. *An illustration of the sector element, R, the gyroradius, r_g and the sector angle, φ. The half circle illustrates the electron cyclotron motion.*

structures [89, 108]. In Paper VI, this feature allowed the imaging of individual droplets from a diesel injector.

In certain applications, the transport or manipulation of x-ray beams using x-ray optics is necessary, for example, in x-ray absorption spectroscopy for warm dense matter [18, 19]. However, as divergence increases, x-ray optics become less efficient, causing a reduction in photon flux [109]. Additionally, for divergent x-ray beams, the S/N decreases with increased propagation distance. To address these challenges, producing low divergence x-rays is crucial and is achievable with an overdense PL [110]. As in LWFA-radiation methods, narrow x-ray beams are emitted within the PL because of the electron deflection caused by the self-generated azimuthal magnetic field, illustrated in Figure 5.1 c). Consequently, the focusing of electrons within the bunch leads to the second emission event producing low-divergence x-rays. This concept was studied in Paper II and Paper IV. The laser pulse co-propagates with the electron bunch from the LWFA, and is intense enough to ionize the PL gas, but not excite a nonlinear wake. Conversely, the electron bunch is dense enough to generate a B_θ strong enough to deflect the off-axis electrons, but still fulfills the condition $n_\mathrm{b} < n_\mathrm{e}$.

The radius of curvature of the electron trajectory as a result of the magnetic field described in the previous section leads to a deflection radius that can be described by the electron cyclotron motion. The gyration motion leads to x-ray emission with specific directionality, divergence, and energy characteristics. The angular frequency of this motion for a relativistic particle is described by the gyration frequency [26]:

$$\omega_\mathrm{g} = \frac{q_e B_\theta}{\gamma m_\mathrm{e}}. \tag{5.7}$$

It is clear from this equation that higher-energetic particles will have a smaller gyration frequency, because of the relativistic mass increase. For simplicity, assume a static magnetic field; then the gyroradius is described by:

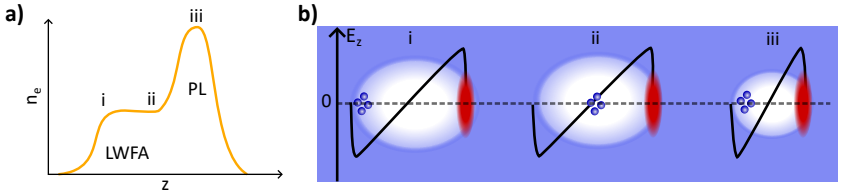

Figure 5.5. *Principle of rephasing. a) illustrates a density profile that can rephase the electron bunch, shown in b). The black line is the accelerating electric field, E_z and the dashed line is included as a guide for $E_z = 0$. At the beginning (i) of the acceleration, the electron bunch is positioned close to the rear of the bubble, experiencing the strongest accelerating field. After the dephasing length (ii), the electrons are positioned at the midpoint of the bubble, now starting to decelerate. In the upramp to the "PL", the bubble contracts, and the electrons are yet again in an accelerating phase (iii).*

$$r_{\mathrm{g}} = \frac{\gamma m_{\mathrm{e}} c}{q_e B_\theta}. \tag{5.8}$$

The gyroradius is illustrated in Figure 5.4. The angular frequency corresponds to the time it takes for the particle to complete one revolution. The maximum sector length is approximately the length of the plasma lens, and the sector angle is given by $\varphi = R/r_{\mathrm{g}}$.

Experimentally, the PL is the 1 mm supersonic gas jet, placed 1 mm above the optical axis, leading to a super Gaussian density profile seen by the laser pulse and electron bunch. Thus, with the above example, using the same bunch as before, with a $\gamma \approx 300$, the radius of curvature becomes 6 mm. The maximum sector length is given by the diameter of the orifice, which leads to a sector angle $\varphi \approx 0.17$ rad. This means that the electrons within the bunch that experience the strongest deflection complete only a partial revolution. This principle is what leads to the focusing of the electrons, and subsequent emission of low-divergence x-rays. Due to the relativistic energies of the electrons, a few hundred γ, and the restricted oscillation, the divergence approaches the incoherent limit, $\theta \approx 1/\gamma$, as demonstrated in Paper IV.

5.2 Rephasing

Chapter 3 discussed that the group velocity of the laser pulse is less than c in the plasma, while the electron bunch propagates with a speed close to c. Consequently, the whole bubble propagates at a slower speed than the electron bunch, leading to dephasing, as discussed in Chapter 4. Eventually, the electron bunch outruns the laser pulse and is exposed to a decelerating phase of the bubble. To counteract this, the plasma density profile can be tailored to increase at the end of the acceleration. Since the plasma wavelength scales inversely with the electron density,

$\lambda_p \propto 1/\sqrt{n_e}$, the plasma bubble thus contracts. Or another way to view this is that the rear of the bubble speeds up, so that the electron bunch is again positioned in the accelerating phase [22, 111]. The principle is experimentally realized by placing a second plasma jet immediately after the LWFA stage, with a background electron density higher than that of the LWFA. High laser pulse intensity is required in the second jet to sustain nonlinear wake excitation during the density upramp.

Figure 5.5 illustrates the principle. The density profile consists of a merged LWFA and PL, Figure 5.5a). Figure 5.5b) shows the electron bunch and bubble evolution throughout the density profile in a), with each position of interest, (i)-(iii) marked above each bubble picture. The black sawtooth lines illustrate the accelerating field, E_z, along the bubble. In this picture, the laser pulse is assumed to be non-evolving for simplicity. At position (i), the electrons are at the back of the bubble and accelerate, until dephasing is reached at position (ii). Here, the electrons experience a strong decelerating field from the leading edge of the bubble and a positive field at the back half of the bubble. At this point, they start to decelerate. In the density region of position (iii), the bubble contracts, so that the electrons are yet again positioned at the back of the bubble and exposed to the accelerating field.

In Paper I, the rephasing stage is integrated with the PL. The study revealed that rephasing and lensing effects can be achieved using an identical configuration. The primary role of the PL is mainly determined by the diffraction of the laser pulse. To maintain rephasing operation, the laser pulse intensity must be sufficiently high to consistently excite a wake during the density transition. This can only occur if the two jets are positioned close enough to each other. At greater distances, the lensing is the dominating effect, since the laser pulse has diffracted too much to drive a nonlinear wake. Thus, by carefully designing the plasma density profile, rephasing can significantly enhance the final energy of the electron bunches in LWFA.

5.3 Spatiotemporal laser pulse steering of electron bunches and x-rays

Understanding and controlling laser spatiotemporal couplings (STC) is critical for precise beam steering in LWFA-based accelerators. In Paper V, the effect of STC on electron bunch and x-ray steering is evaluated. In Chapter 2, a laser pulse without STC was described, $U(\mathbf{r}, t) = U(r) \cdot U(t)$. For a laser pulse with STC, this separation of variables is not possible; that is, $U(\mathbf{r}, t) \neq U(r) \cdot U(t)$. The effect can have detrimental consequences for pulses in the sub-10 fs regime, such as the OPCPA laser described in Chapter 2 [112]. In the experiment presented in Paper V, STC is introduced by misaligning the grating compressor of the LLC multi-TW Ti:sapphire CPA laser, as illustrated

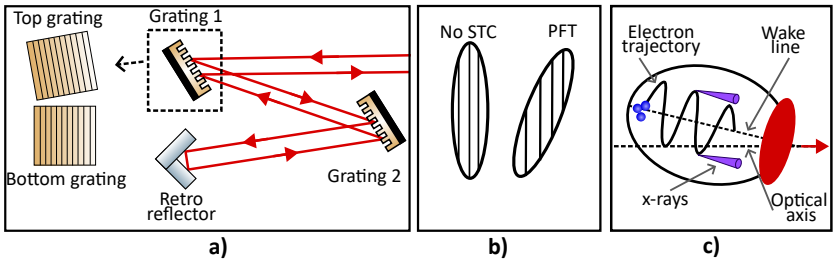

Figure 5.6. *A summary of STC, and the effects on LWFA. a) a sketch of the LLC multi-TW CPA Ti:sapphire grating compressor. Grating 1 and grating 2 are aligned with each other, so the grating surfaces are parallel. Grating 2 is one large grating, and grating 1 is made up of two smaller stacked gratings. The top grating is adjusted so that it can be rotated in a plane, as shown in the figure. b) illustration of a laser pulse with no STC compared to a pulse with PFT. In both cases, the wavefront remains parallel to the propagation direction. c) the effects of PFT on LWFA. The optical axis denotes the laser pointing, and the wakeline denotes the center of the excited bubble. The electrons and subsequent x-rays follow the wakeline.*

in Figure 5.6 a), which shows a schematic of the grating compressor. Grating 1 is made up of two gratings stacked on top of each other, and grating 2 is one large grating. An STC-free grating compressor has parallel gratings, with aligned grooves. With grating 1, STC can be introduced in a controlled way by rotating the top grating in plane, shown in the figure as a rotation with respect to the bottom grating. This type of misalignment introduces an angular chirp and manifests itself as a pulse-front tilt (PFT) in the beam leaving the compressor, as shown in Figure 5.6 b), where two beams are illustrated. In essence, a PFT means that different parts of the laser pulse arrive at different times across the transverse profile. When no STC is present, the wavefront, illustrated by the vertical lines within the ovals, is aligned with the temporal envelope and both are orthogonal to the propagation vector. In cases where PFT is present, the pulse intensity profile is tilted relative to the optical axis, but the wavefront remains orthogonal to it. A consequence of the PFT is that the wake excitation is angularly displaced with respect to the optical axis, illustrated in Figure 5.6 c). The wakeline is defined as the axis at which the radial electric and magnetic fields cancel, which is at the radial center of the bubble. With no STC, the wakeline coincides with the optical axis. The electron bunch oscillates around this point within the bubble, and the x-rays are emitted around this axis as well. Evidently, the PFT causes the electron bunch to steer off the optical axis [25, 113, 114]. In Paper V we showed that the x-rays follow this path with perfect correlation to the electron pointing. The knowledge of this effect is important for applications, calibration of electron spectrometers, and staging. Fine-tuning of the grating compressor alignment was implemented in Paper II and Paper IV to steer the low-divergence x-rays

to the detector, highlighting the importance of both laser beam path and beam quality control. Accurate grating alignment is therefore essential not only for optimal laser compression but also for ensuring controlled electron and x-ray beam propagation.

Chapter summary

A multitude of experimental and theoretical studies have been conducted on underdense plasma lenses. This area is intriguing because of ongoing research into LWFA-based injectors for FELs and staging. Overdense plasma lenses enable efficient focusing of electron bunches and generation of narrow x-ray beams. Rephasing through density tailoring allows energy gain beyond the dephasing limit. The PL described in this chapter is straightforward to implement experimentally, and the scheme has proven to be robust. Another important parameter for beam control is the STC of the laser pulse, which causes off-axis wake excitations and steers the generated beams away from the optical axis. Precise control of spatio-temporal couplings is necessary for accurate beam steering and staging in LWFA.

Chapter 6

Summary and outlook

Looking ahead, several exciting opportunities remain for further advancing LWFA technologies. The development of LWFA is progressing rapidly, with larger facilities all over the world dedicated to the technique [115]. Today, LWFA does not replace conventional rf accelerators, but is a strong complement to the technique, offering unique radiation properties that are not easily accessible at conventional acceleration facilities. Harnessing the strength of both machines, by combining them, such as LWFA injectors for FELs [24, 103, 116, 117], or staging LWFA with conventional accelerators through LWFA-PWFA schemes, opens new avenues for previously unexplored physics. Already, LWFA electrons have been used in an extended beam line, using conventional magnetic optics [91, 118].

The short pulse, high repetition rate regime, available by novel laser systems, such as the OPCPA, significantly enhances the capabilities of LWFA: high-repetition pump probe experiments [119] are possible with increased knowledge, stability, and control of the LWFA process. In theory, the repetition rate of such an experiment is limited only by the fundamental recovery time of the plasma [120], which is the time it takes for the plasma to be considered neutral before the next acceleration cycle starts. Controlled injection and trapping, through shock-front injection, and the few-cycle laser regime lead to the LWFA extending into the attosecond regime [121, 122], where ultra-fast electron dynamics can be studied.

This thesis advances the stability and control of LWFA, without complicated schemes, thus preserving the machine's compactness. In Chapter 4, robust injection methods are discussed, and the most successful scheme which continues to produce narrow

quasi-monoenergetic electron bunches is shock-assisted ionization injection. Chapter 5 of this thesis highlights the feasibility and flexibility of plasma lenses or additional plasma profiles. The plasma lens operates primarily in the overdense regime, where its lensing effect depends on the bunch density rather than the background plasma electron density. This leads to the strength of the lens being not externally controllable, as it depends on the conditions under which the driving electron bunch was generated. However, with increased control of injection and trapping, the lensing effect also becomes fully controllable. As a consequence, because of the deflection of the electrons by the strong self-generated azimuthal magnetic field, x-rays are subsequently emitted. These x-rays are approaching the incoherent limit and have a significant photon yield. This compact x-ray source greatly adds to the possible applications of LWFA-produced radiation, readily available in high-power laser laboratories, thus complementing research areas that currently rely on conventional rf accelerator facilities. With a setup similar to the plasma lens, it has been shown that the dephasing length of LWFA can be overcome, boosting the energy gain of the electron bunches.

The work presented in this thesis demonstrates that LWFA can be effectively controlled to a great extent by controlling the drive laser pulse and plasma parameters. The presented schemes show great flexibility, are easily implemented experimentally, and greatly improve the LWFA beam quality.

The author's contributions

I **Combined plasma lens and rephasing stage for a laser wakefield accelerator**
In this paper, several techniques are combined to produce quasi-monoenergetic electron bunches. A second, high-density region is used to boost the energy of the electron bunch and to reduce the transverse divergence. I planned the experiment, jointly built the setup, and acquired the data. I analyzed all data and prepared the manuscript.

II **Collimated x-rays emitted through laser-driven plasma lensing**
Collimated x-rays from a high-density plasma lens are observed. I planned the experiment, jointly built the setup, and acquired the data. I analyzed all data and prepared the manuscript.

III **Plasma density profile reconstruction of a gas cell for ionization induced laser wakefield acceleration**
A single shot, accurate reconstruction of the plasma density within a gas cell, which combines interferogram with shadowgraphy. I jointly planned the experiment, built the setup and acquired the data. I reviewed and provided feedback on the manuscript.

IV **Parametric study of low-divergence x-ray generation from a laser-plasma accelerator using an overdense plasma lens**
A parametric study of low-divergence x-rays emitted from a high-density plasma lens is observed. I planned the experiment, jointly built the setup, and acquired the data. I analyzed all data and prepared the manuscript.

V **Correlating optical pulse-front tilt steering of X-ray and electron pulses from laser wakefield accelerators**
The correlation between laser spatiotemporal couplings, electrons, and x-rays is studied. I jointly planned the experiment, built the setup and acquired data. I reviewed and provided feedback on the manuscript.

VI **Spatiotemporal distribution of liquid mass from spray M using x-ray tomography driven by a laser plasma accelerator**
The time evolution of the ECN spray M nozzle is characterized using x-rays from LWFA. By recording the spray at a fixed time, from different angles, a 3D reconstruction is made. I jointly planned the experiment, built the setup and acquired the data. I co-wrote the method section and reviewed the manuscript.

Acknowledgments

I can't believe that I'm a thesis richer, and that I still need to do a Google search on how to calculate the volume of anything other than a cube. With that said, several people have been involved in my work and education during these years, and I will most likely forget someone, given that I'm writing in mid-delirium. But just know that even if you are not mentioned, I'm still very thankful for you.

To Dr. Olle Lundh, my main supervisor, thanks for your support. To my co-supervisor, Per Eng-Johnsson, for your support and for always having my back in teaching matters.

I would like to thank my team, old members and current: To Claes-Göran Wahlström for always having your door open for my questions or concerns, and your support through my years at the division and on my projects; Andrea Angella for being a great office pal and always having a positive attitude; Erik Löfquist, I seriously adore you, thanks for being a great teammate and for your patience (with me, in case you did not catch that); Flanish D'Souza for being easy to work with; Jonas Björklund Svensson, for your support, starting already during my master's thesis, your feedback always means a lot; Kristoffer Svendsen, the office is not quite the same without you, thanks for the many hours of fun lab work; Alexander Permogorov, you are my fire.

To Anders Persson, thanks for keeping your end of our deal — I don't think this thesis could have been written without you. Everything I know about the lab I owe to you. Thanks for being a fair morning competitor. I am willing to admit my defeat.

Across the laser room: Marius Plack, Venús Poulain, and Elisa Appi, for letting me roam free on my scavenge hunts. I think Marius has been good at marking everything up, so stuff will return to you eventually. :)

Within this thesis, I have had the privilege to work with collaborators from all over the world, and I'm thankful to all of you. I would like to express a special thanks to those who influenced my work the most. To Lewis Dickson, for always having my back. Michael Backhouse for patiently replying to my emails and for all the laughs, thank you. Jonathan Wood, Brendan Kettle, and Matt Streeter, I had a great time at Gemini and most of that is thanks to how you ran the experiment.

Thanks to all my colleagues at the division of Atomic Physics, for insightful discussions and great lunch company. I want to say a special thanks to my false cousin, David Gustavsson, I know that you're truly a "northerner". Marcus Lindén, you have a way of always lifting my mood. Antonious Renders, I'm just so grateful that you exist. Maria Ruchkina, I think you might be one of the most badass people I've ever met, thanks for cheering me on. Akvilé Zabiliute-Karaliune, for always being so thoughtful and supportive. To Adam Kinos, thanks for always offering a helping hand. Thanksan, Anne-Lisesan Viotti, I've absolutely loved teaching with you. Thanks for your readiness to lend a listening ear, and many hours of food discussion. Saga Westerberg, I'm trying to pick one thing (and it's difficult), so this gratitude will probably look horrible; but I'm so glad to have met you. Carolina Juliano, Marzo López Cerón, and Isa Clementson; you are all great young researchers, and I know that you have bright paths ahead of you. To Åke Johansson, thanks for always solving a huge part of my problems, which involves my computer. To Maria Algotsson, thanks for helping me with my purchases and letting me vent about house troubles. Thank you both for many years of sane lunch company.

To my family, biological and extended. To my friends. Thanks for all your support.

Emily Archer, I found a piece of myself when I met you. Annabel Gunn, I adore you so much and love our midnight deliriums. To the best awkward cheerleader, Love Kildetoft. Thanks for being in my awkward corner. To Emma Simpson, thanks for always listening to my concerns.

Giada Cantono, I cannot express in words how much your support means to me. You gave me the confidence early in my career that I needed to succeed. You have been, and still are, an integral part of my life.

Last but not least, I would like to thank my better half, Marc Nilsson. I could not have done this without you and Mitzi.

References

1. P. J. Bryant. *A brief history and review of accelerators.* CAS - CERN Accelerator School : 5th General Accelerator Physics Course pages 1–16 (1994).

2. IAEA. *More background on accelerators.* URL `https://www.iaea.org/topics/nuclear-science/nuclear-research/accelerators/background`.

3. *The Large Hadron Collider — CERN.* URL `https://home.cern/science/accelerators/large-hadron-collider`.

4. T. Tajima and J. M. Dawson. *Laser Electron Accelerator.* Physical Review Letters **43**, 267 (1979).

5. D. Strickland and G. Mourou. *Compression of amplified chirped optical pulses.* Optics Communications **55**, 447–449 (1985).

6. A. Modena, Z. Najmudin, A. E. Dangor, C. E. Clayton, K. A. Marsh, C. Joshi, V. Malka, C. B. Darrow, C. Danson, D. Neely and F. N. Walsh. *Electron acceleration from the breaking of relativistic plasma waves.* Nature 1995 377:6550 **377**, 606–608 (1995).

7. J. Faure, Y. Glinec, A. Pukhov, S. Klselev, S. Gordienko, E. Lefebvre, J. P. Rousseau, F. Burgy and V. Malka. *A laser–plasma accelerator producing monoenergetic electron beams.* Nature 2004 431:7008 **431**, 541–544 (2004).

8. C. G. Geddes, C. Toth, J. Van Tilborg, E. Esarey, C. B. Schroeder, D. Bruhwiler, C. Nieter, J. Cary and W. P. Leemans. *High-quality electron beams from a laser wakefield accelerator using plasma-channel guiding.* Nature 2004 431:7008 **431**, 538–541 (2004).

9. S. P. Mangles, C. D. Murphy, Z. Najmudin, A. G. Thomas, J. L. Collier, A. E. Dangor, E. J. Divall, P. S. Foster, J. G. Gallacher, C. J. Hooker, D. A. Jaroszynski, A. J. Langley, W. B. Mori, P. A. Norreys, F. S. Tsung, R. Viskup, B. R. Walton and K. Krushelnick. *Monoenergetic beams of relativistic electrons from intense laser–plasma interactions.* Nature 2004 431:7008 **431**, 535–538 (2004).

10. A. Pukhov, S. Kiselev, I. Kostyukov and J. Meyer-ter Vehn. *Laser wake field acceleration in bubble regime: quasi-monoenergetic electron bunches and flashes of synchrotron radiation.* page 345 (2003).

11. V. Malka, J. Faure, Y. Glinec, A. Pukhov and J. P. Rousseau. *Monoenergetic electron beam optimization in the bubble regime.* Physics of Plasmas **12**, 1–8 (2005).

12. X. Wang, R. Zgadzaj, N. Fazel, Z. Li, S. A. Yi, X. Zhang, W. Henderson, Y. Y. Chang, R. Korzekwa, H. E. Tsai, C. H. Pai, H. Quevedo, G. Dyer, E. Gaul, M. Martinez, A. C. Bernstein, T. Borger, M. Spinks, M. Donovan, V. Khudik, G. Shvets, T. Ditmire and M. C. Downer. *Quasi-monoenergetic laser-plasma acceleration of electrons to 2GeV.* Nature Communications 2013 4:1 **4**, 1–9 (2013).

13. O. Lundh, J. Lim, C. Rechatin, L. Ammoura, A. Ben-Ismaïl, X. Davoine, G. Gallot, J. P. Goddet, E. Lefebvre, V. Malka and J. Faure. *Few femtosecond, few kiloampere electron bunch produced by a laser–plasma accelerator.* Nature Physics 2010 7:3 **7**, 219–222 (2011).

14. S. Corde, K. T. Phuoc, G. Lambert, R. Fitour, V. Malka, A. Rousse, A. Beck and E. Lefebvre. *Femtosecond x rays from laser-plasma accelerators.* Reviews of Modern Physics **85**, 1 (2013).

15. K. Falk, M. Šmíd, K. Boháček, U. Chaulagain, Y. Gu, X. Pan, P. Perez-Martin, M. Krůs and M. Kozlová. *Laser-driven low energy electron beams for single-shot ultra-fast probing of meso-scale materials and warm dense matter.* Scientific Reports 2023 13:1 **13**, 1–9 (2023).

16. A. E. Hussein, N. Senabulya, Y. Ma, M. J. Streeter, B. Kettle, S. J. Dann, F. Albert, N. Bourgeois, S. Cipiccia, J. M. Cole, O. Finlay, E. Gerstmayr, I. G. González, A. Higginbotham, D. A. Jaroszynski, K. Falk, K. Krushelnick, N. Lemos, N. C. Lopes, C. Lumsdon, O. Lundh, S. P. Mangles, Z. Najmudin, P. P. Rajeev, C. M. Schlepütz, M. Shahzad, M. Smid, R. Spesyvtsev, D. R. Symes, G. Vieux, L. Willingale, J. C. Wood, A. J. Shahani and A. G. Thomas. *Laser-wakefield accelerators for high-resolution X-ray imaging of complex microstructures.* Scientific Reports 2019 9:1 **9**, 1–13 (2019).

17. B. J. Jensen, S. N. Luo, D. E. Hooks, K. Fezzaa, K. J. Ramos, J. D. Yeager, K. Kwiatkowski, T. Shimada and D. M. Dattelbaum. *Ultrafast, high resolution, phase contrast imaging of impact response with synchrotron radiation.* AIP Advances **2**, 12170 (2012).

18. B. Kettle, E. Gerstmayr, M. Streeter, F. Albert, R. Baggott, N. Bourgeois, J. Cole, S. Dann, K. Falk, I. Gallardo González, A. Hussein, N. Lemos, N. Lopes, O. Lundh, Y. Ma, S. Rose, C. Spindloe, D. Symes, M. Šmíd, A. Thomas, R. Watt and S. Mangles. *Single-Shot Multi-keV X-Ray Absorption Spectroscopy Using an Ultrashort Laser-Wakefield Accelerator Source.* Physical Review Letters **123**, 254801 (2019).

19. B. Mahieu, N. Jourdain, K. Ta Phuoc, F. Dorchies, J. P. Goddet, A. Lifschitz, P. Renaudin and L. Lecherbourg. *Probing warm dense matter using femtosecond X-ray absorption spectroscopy with a laser-produced betatron source.* Nature Communications 2018 9:1 **9**, 1–6 (2018).

20. M. Z. Mo, Z. Chen, S. Fourmaux, A. Saraf, S. Kerr, K. Otani, R. Masoud, J.-C. Kieffer, Y. Tsui, A. Ng and R. Fedosejevs. *Measurements of ionization states in warm dense aluminum with betatron radiation.* Physical Review E **95**, 053208 (2017).

21. J. C. Wood, D. J. Chapman, K. Poder, N. C. Lopes, M. E. Rutherford, T. G. White, F. Albert, K. T. Behm, N. Booth, J. S. Bryant, P. S. Foster, S. Glenzer, E. Hill, K. Krushelnick, Z. Najmudin, B. B. Pollock, S. Rose, W. Schumaker, R. H. Scott, M. Sherlock, A. G. Thomas, Z. Zhao, D. E. Eakins and S. P. Mangles. *Ultrafast Imaging of Laser Driven Shock Waves using Betatron X-rays from a Laser Wakefield Accelerator.* Scientific Reports 2018 8:1 **8**, 1–10 (2018).

22. A. Döpp, E. Guillaume, C. Thaury, A. Lifschitz, K. T. Phuoc and V. Malka. *Energy boost in laser wakefield accelerators using sharp density transitions.* Physics of Plasmas **23**, 056702 (2015).

23. C. E. Doss, E. Adli, R. Ariniello, J. Cary, S. Corde, B. Hidding, M. J. Hogan, K. Hunt-Stone, C. Joshi, K. A. Marsh, J. B. Rosenzweig, N. Vafaei-Najafabadi, V. Yakimenko and M. Litos. *Laser-ionized, beam-driven, underdense, passive thin plasma lens.* Physical Review Accelerators and Beams **22**, 111001 (2019).

24. K. Nakajima. *Towards a table-top free-electron laser.* Nature Physics **4**, 92–93 (2008).

25. M. Thévenet, D. E. Mittelberger, K. Nakamura, R. Lehe, C. B. Schroeder, J.-L. Vay, E. Esarey and W. P. Leemans. *Pulse front tilt steering in laser plasma accelerators.* Physical Review Accelerators and Beams **22**, 071301 (2019).

26. J. Jackson. *Classical Electrodynamics* (1999). John Wiley & Sons, Limited Hoboken 3rd edition. ISBN 978-0-471-30932-1.

27. D. J. Griffiths. *Introduction to Electrodynamics* (2017). Cambridge University Press 4 edition. ISBN 9781108333511.

28. P. Gibbon. *Short pulse laser interactions with matter: An introduction* (2005). Imperial College Press London 1 edition. ISBN 1-86094-135-4.

29. B. E. A. Saleh and M. C. Teich. *Fundamentals of Photonics* (1991). John Wiley & Sons, Inc. New York, USA. ISBN 0471839655.

30. L. T. Dickson, C. I. Underwood, F. Filippi, R. J. Shalloo, J. B. Svensson, D. Guénot, K. Svendsen, I. Moulanier, S. D. Dufrénoy, C. D. Murphy, N. C. Lopes, P. P. Rajeev, Z. Najmudin, G. Cantono, A. Persson, O. Lundh, G. Maynard, M. J. Streeter and B. Cros. *Mechanisms to control laser-plasma coupling in laser wakefield electron acceleration.* Physical Review Accelerators and Beams **25**, 101301 (2022).

31. A. Buck, K. Zeil, A. Popp, K. Schmid, A. Jochmann, S. D. Kraft, B. Hidding, T. Kudyakov, C. M. Sears, L. Veisz, S. Karsch, J. Pawelke, R. Sauerbrey, T. Cowan, F. Krausz and U. Schramm. *Absolute charge calibration of scintillating screens for relativistic electron detection.* Review of Scientific Instruments **81**, 033301 (2010).

32. R. D. Small, V. A. Sernas and R. H. Page. *Single Beam Schlieren Interferometer Using a Wollaston Prism.* Applied Optics **11**, 858 (1972).

33. R. Benattar, C. Popovics and R. Sigel. *Polarized light interferometer for laser fusion studies.* Review of Scientific Instruments **50**, 1583–1586 (1979).

34. A. Howard, D. Haberberger, R. Boni, R. Brown and D. H. Froula. *Implementation of a Wollaston interferometry diagnostic on OMEGA EP.* Review of Scientific Instruments **89**, 10–107 (2018).

35. F. Brandi and L. A. Gizzi. *Optical diagnostics for density measurement in high-quality laser-plasma electron accelerators.* High Power Laser Science and Engineering **7**, e26 (2019).

36. J. Glasser, J. Chapelle and J. C. Boettner. *Abel inversion applied to plasma spectroscopy: a new interactive method.* Applied Optics **17**, 3750 (1978).

37. J. P. Couperus, A. Köhler, T. A. Wolterink, A. Jochmann, O. Zarini, H. M. Bastiaens, K. J. Boller, A. Irman and U. Schramm. *Tomographic characterisation of gas-jet targets for laser wakefield acceleration.* Nuclear Instruments and Methods in Physics Research, Section A: Accelerators, Spectrometers, Detectors and Associated Equipment **830**, 504–509 (2016).

38. D. D. Hickstein, S. T. Gibson, R. Yurchak, D. D. Das and M. Ryazanov. *A direct comparison of high-speed methods for the numerical Abel transform.* Review of Scientific Instruments **90**, 65115 (2019).

39. G. Pretzler. *A New Method for Numerical Abel-Inversion.* Zeitschrift fur Naturforschung - Section A Journal of Physical Sciences **46**, 639–641 (1991).

40. S. Lee, I. Nam, M. Cho, D. Jang, S. Kwon, H. Suk and M. Kim. *Interferometry analysis with fringe normalization and matrix Abel inversion for plasma diagnostics.* Journal of Instrumentation **18**, C12016 (2023).

41. K. Staszek and M. Bogusz. *Simple Fringe Pattern Normalization Algorithm.* IFAC Proceedings Volumes **45**, 353–356 (2012).

42. E. Esarey, C. B. Schroeder and W. P. Leemans. *Physics of laser-driven plasma-based electron accelerators.* Reviews of Modern Physics **81**, 1229–1285 (2009).

43. S. Kneip, C. McGuffey, J. L. Martins, S. F. Martins, C. Bellei, V. Chvykov, F. Dollar, R. Fonseca, C. Huntington, G. Kalintchenko, A. Maksimchuk, S. P. D. Mangles, T. Matsuoka, S. R. Nagel, C. A. J. Palmer, J. Schreiber, K. T. Phuoc, A. G. R. Thomas, V. Yanovsky, L. O. Silva, K. Krushelnick and Z. Najmudin. *Bright spatially coherent synchrotron X-rays from a table-top source.* Nature Physics **6**, 980–983 (2010).

44. A. Pukhov, S. Gordienko, S. Kiselev and I. Kostyukov. *The bubble regime of laser–plasma acceleration: monoenergetic electrons and the scalability.* Plasma Physics and Controlled Fusion **46**, B179–B186 (2004).

45. P. Mulser and D. Bauer. *High Power Laser-Matter Interaction* (2010) volume 238 of *Springer Tracts in Modern Physics*. Springer Berlin Heidelberg Berlin, Heidelberg. ISBN 978-3-540-50669-0.

46. W. Lu, M. Tzoufras, C. Joshi, F. S. Tsung, W. B. Mori, J. Vieira, R. A. Fonseca and L. O. Silva. *Generating multi-GeV electron bunches using single stage laser wakefield acceleration in a 3D nonlinear regime.* Physical Review Special Topics - Accelerators and Beams **10**, 061301 (2007).

47. C. D. Decker, W. B. Mori, K. C. Tzeng and T. Katsouleas. *The evolution of ultra-intense, short-pulse lasers in underdense plasmas.* Physics of Plasmas **3**, 2047–2056 (1996).

48. J. Faure, Y. Glinec, J. J. Santos, F. Ewald, J.-P. Rousseau, S. Kiselev, A. Pukhov, T. Hosokai and V. Malka. *Observation of Laser-Pulse Shortening in Nonlinear Plasma Waves.* Physical Review Letters **95**, 205003 (2005).

49. H. Ding, A. Döpp, M. Gilljohann, J. Götzfried, S. Schindler, L. Wildgruber, G. Cheung, S. M. Hooker and S. Karsch. *Nonlinear plasma wavelength scalings in a laser wakefield accelerator.* Physical Review E **101**, 023209 (2020).

50. J. Götzfried, A. Döpp, M. F. Gilljohann, F. M. Foerster, H. Ding, S. Schindler, G. Schilling, A. Buck, L. Veisz and S. Karsch. *Physics of High-Charge Electron Beams in Laser-Plasma Wakefields.* Physical Review X **10**, 041015 (2020).

51. S. Bulanov, N. Naumova, F. Pegoraro and J. Sakai. *Particle injection into the wave acceleration phase due to nonlinear wake wave breaking.* Physical Review E **58**, R5257–R5260 (1998).

52. M. Chen, Z.-M. Sheng, Y.-Y. Ma and J. Zhang. *Electron injection and trapping in a laser wakefield by field ionization to high-charge states of gases.* Journal of Applied Physics **99**, 056109 (2006).

53. A. Pak, K. A. Marsh, S. F. Martins, W. Lu, W. B. Mori and C. Joshi. *Injection and trapping of tunnel-ionized electrons into laser-produced wakes.* Physical Review Letters **104**, 025003 (2010).

54. C. E. Clayton, J. E. Ralph, F. Albert, R. A. Fonseca, S. H. Glenzer, C. Joshi, W. Lu, K. A. Marsh, S. F. Martins, W. B. Mori, A. Pak, F. S. Tsung, B. B. Pollock, J. S. Ross, L. O. Silva and D. H. Froula. *Self-guided laser wakefield acceleration beyond 1 GeV using ionization-induced injection.* Physical Review Letters **105**, 105003 (2010).

55. M. S. Bloom, M. J. V. Streeter, S. Kneip, R. A. Bendoyro, O. Cheklov, J. M. Cole, A. Döpp, C. J. Hooker, J. Holloway, J. Jiang, N. C. Lopes, H. Nakamura, P. A. Norreys, P. P. Rajeev, D. R. Symes, J. Schreiber, J. C. Wood, M. Wing, Z. Najmudin and S. P. D. Mangles. *Bright x-ray radiation from plasma bubbles in an evolving laser wakefield accelerator.* Physical Review Accelerators and Beams **23** (2020).

56. K. Schmid and L. Veisz. *Supersonic gas jets for laser-plasma experiments.* Review of Scientific Instruments **83** (2012).

57. A. Buck, J. Wenz, J. Xu, K. Khrennikov, K. Schmid, M. Heigoldt, J. M. Mikhailova, M. Geissler, B. Shen, F. Krausz, S. Karsch and L. Veisz. *Shock-Front Injector for High-Quality Laser-Plasma Acceleration.* Physical Review Letters **110**, 185006 (2013).

58. C. Thaury, E. Guillaume, A. Lifschitz, K. Ta Phuoc, M. Hansson, G. Grittani, J. Gautier, J.-P. Goddet, A. Tafzi, O. Lundh and V. Malka. *Shock assisted ionization injection in laser-plasma accelerators.* Scientific Reports **5**, 16310 (2015).

59. M. Hansson, T. L. Audet, H. Ekerfelt, B. Aurand, I. Gallardo González, F. G. Desforges, X. Davoine, A. Maitrallain, S. Reymond, P. Monot, A. Persson, S. Dobosz Dufrénoy, C. G. Wahlström, B. Cros and O. Lundh. *Localization of ionization-induced trapping in a laser wakefield accelerator using a density down-ramp.* Plasma Physics and Controlled Fusion **58**, 055009 (2016).

60. J. P. Couperus Cabada˘, R. Pausch, S. Schöbel, M. Bussmann, Y.-Y. Chang, S. Corde, A. Debus, H. Ding, A. Döpp, F. M. Foerster, M. Gilljohann, F. Haberstroh, T. Heinemann, B. Hidding, S. Karsch, A. Koehler, O. Kononenko, A. Knetsch, T. Kurz, A. Martinez De La Ossa, A. Nutter, G. Raj, K. Steiniger, U. Schramm, P. Ufer and A. Irman. *Gas-dynamic density downramp injection in a beam-driven plasma wakefield accelerator.* Physical Review Research **3**, 42005 (2005).

61. D. E. Cardenas, S. Chou, E. Wallin, J. Xu, L. Hofmann, A. Buck, K. Schmid, D. E. Rivas, B. Shen, A. Gonoskov, M. Marklund and L. Veisz. *Electron bunch evolution in laser-wakefield acceleration.* Physical Review Accelerators and Beams **23**, 112803 (2020).

62. K. v. Grafenstein, F. M. Foerster, F. Haberstroh, D. Campbell, F. Irshad, F. C. Salgado, G. Schilling, E. Travac, N. Weiße, M. Zepf, A. Döpp and S. Karsch. *Laser-accelerated electron beams at 1 GeV using optically-induced shock injection.* Scientific Reports **13** (2023).

63. O. Girin. *Dynamics of Compressible Fluids* (2022). Springer International Publishing Cham. ISBN 978-3-031-11261-4.

64. K. Schmid, A. Buck, C. M. Sears, J. M. Mikhailova, R. Tautz, D. Herrmann, M. Geissler, F. Krausz and L. Veisz. *Density-transition based electron injector for laser driven wakefield accelerators.* Physical Review Special Topics - Accelerators and Beams **13** (2010).

65. A. Pukhov and I. Kostyukov. *Control of laser-wakefield acceleration by the plasma-density profile.* Physical Review E **77**, 025401 (2008).

66. T. Ohkubo, A. Zhidkov, T. Hosokai, K. Kinoshita and M. Uesaka. *Effects of density gradient on short-bunch injection by wave breaking in the laser wake field acceleration.* Physics of Plasmas **13** (2006).

67. L. Rovige, J. Huijts, I. Andriyash, A. Vernier, V. Tomkus, V. Girdauskas, G. Raciukaitis, J. Dudutis, V. Stankevic, P. Gecys, M. Ouille, Z. Cheng, R. Lopez-Martens and J. Faure. *Demonstration of stable long-term operation of a kilohertz laser-plasma accelerator.* Physical Review Accelerators and Beams **23**, 093401 (2020).

68. P. Sprangle, B. Hafizi, J. R. Peñano, R. F. Hubbard, A. Ting, C. I. Moore, D. F. Gordon, A. Zigler, D. Kaganovich and T. M. Antonsen. *Wakefield generation and GeV acceleration in tapered plasma channels.* Physical Review E **63**, 056405 (2001).

69. H. Ekerfelt, M. Hansson, I. Gallardo González, X. Davoine and O. Lundh. *A tunable electron beam source using trapping of electrons in a density down-ramp in laser wakefield acceleration.* Scientific Reports 2017 7:1 **7**, 1–9 (2017).

70. A. J. Gonsalves, K. Nakamura, C. Lin, D. Panasenko, S. Shiraishi, T. Sokollik, C. Benedetti, C. B. Schroeder, C. G. Geddes, J. Van Tilborg, J. Osterhoff, E. Esarey, C. Toth and W. P. Leemans. *Tunable laser plasma accelerator based on longitudinal density tailoring.* Nature Physics 2011 7:11 **7**, 862–866 (2011).

71. I. Kostyukov, S. Kiselev and A. Pukhov. *X-ray generation in an ion channel.* Physics of Plasmas **10**, 4818–4828 (2003).

72. S. Kiselev, A. Pukhov and I. Kostyukov. *X-ray Generation in Strongly Nonlinear Plasma Waves.* Physical Review Letters **93**, 135004 (2004).

73. J. Ferri, S. Corde, A. Döpp, A. Lifschitz, A. Doche, C. Thaury, K. Ta Phuoc, B. Mahieu, I. A. Andriyash, V. Malka and X. Davoine. *High-Brilliance Betatron γ-Ray Source Powered by Laser-Accelerated Electrons.* Physical Review Letters **120**, 254802 (2018).

74. A. Rousse, K. T. Phuoc, R. Shah, A. Pukhov, E. Lefebvre, V. Malka, S. Kiselev, F. Burgy, J.-P. Rousseau, D. Umstadter and D. Hulin. *Production of a keV X-Ray Beam from Synchrotron Radiation in Relativistic Laser-Plasma Interaction.* Physical Review Letters **93**, 135005 (2004).

75. F. Albert, R. Shah, K. T. Phuoc, R. Fitour, F. Burgy, J.-P. Rousseau, A. Tafzi, D. Douillet, T. Lefrou and A. Rousse. *Betatron oscillations of electrons accelerated in laser wakefields characterized by spectral x-ray analysis.* Physical Review E **77**, 056402 (2008).

76. A. Köhler, J. P. Couperus, O. Zarini, A. Jochmann, A. Irman and U. Schramm. *Single-shot betatron source size measurement from a laser-wakefield accelerator.* Nuclear Instruments and Methods in Physics Research Section A: Accelerators, Spectrometers, Detectors and Associated Equipment **829**, 265–269 (2016).

77. R. C. Shah, F. Albert, K. Ta Phuoc, O. Shevchenko, D. Boschetto, A. Pukhov, S. Kiselev, F. Burgy, J.-P. Rousseau and A. Rousse. *Coherence-based transverse measurement of synchrotron x-ray radiation from relativistic laser-plasma interaction and laser-accelerated electrons.* Physical Review E **74**, 045401 (2006).

78. K. T. Phuoc, S. Corde, R. Shah, F. Albert, R. Fitour, J.-P. Rousseau, F. Burgy, B. Mercier and A. Rousse. *Imaging Electron Trajectories in a Laser-Wakefield Cavity Using Betatron X-Ray Radiation.* Physical Review Letters **97**, 225002 (2006).

79. A. Döpp, B. Mahieu, A. Lifschitz, C. Thaury, A. Doche, E. Guillaume, G. Grittani, O. Lundh, M. Hansson, J. Gautier, M. Kozlova, J. P. Goddet, P. Rousseau, A. Tafzi, V. Malka, A. Rousse, S. Corde and K. Ta Phuoc. *Stable femtosecond X-rays with tunable polarization from a laser-driven accelerator.* Light: Science & Applications **6**, e17086–e17086 (2017).

80. S. P. Mangles, A. G. Thomas, M. C. Kaluza, O. Lundh, F. Lindau, A. Persson, F. S. Tsung, Z. Najmudin, W. B. Mori, C. G. Wahlström and K. Krushelnick. *Laser-wakefield acceleration of monoenergetic electron beams in the first plasma-wave period.* Physical Review Letters **96**, 215001 (2006).

81. O. J. Finlay, J.-N. Gruse, C. Thornton, R. Allott, C. D. Armstrong, C. D. Baird, N. Bourgeois, C. Brenner, S. Cipiccia, J. M. Cole, C. Gregory, S. Jamison, Y. Katzir, N. C. Lopes, S. P. D. Mangles, C. D. Murphy, Z. Najmudin, D. Neely, L. R. Pickard, K. D. Potter, P. P. Rajeev, D. Rusby, M. P. Selwood, D. R. Symes, C. I. D. Underwood, J. C. Wood, A. G. R. Thomas and M. J. V. Streeter. *Characterisation of a laser plasma betatron source for high resolution x-ray imaging.* Plasma Physics and Controlled Fusion **63**, 084010 (2021).

82. V. Tomkus, V. Girdauskas, J. Dudutis, P. Gečys, V. Stankevič, G. Račiukaitis, I. Gallardo González, D. Guénot, J. B. Svensson, A. Persson and O. Lundh. *Laser wakefield accelerated electron beams and betatron radiation from multijet gas targets.* Scientific Reports 2020 10:1 **10**, 1–17 (2020).

83. P. Kirkpatrick. *Theory and Use of Ross Filters. II.* Review of Scientific Instruments **15**, 223–229 (1944).

84. I. V. Khutoretsky. *Design of an optimal Ross filter system for x-ray spectra measurements in the range of 8.98–88 keV.* Review of Scientific Instruments **66**, 773–775 (1995).

85. *CXRO X-Ray Interactions With Matter.* URL `https://henke.lbl.gov/optical_constants/`.

86. *Solutions Beyond The Visible High Energy Detection.* URL `https://andor.oxinst.com/products/high-energy-detection/ikon-l-so`.

87. C. Fourment, N. Arazam, C. Bonte, T. Caillaud, D. Descamps, F. Dorchies, M. Harmand, S. Hulin, S. Petit and J. J. Santos. *Broadband, high dynamics and high resolution charge coupled device-based spectrometer in dynamic mode for multi-keV repetitive x-ray sources.* Review of Scientific Instruments **80**, 83505 (2009).

88. D. Guénot, K. Svendsen, J. Björklund Svensson, H. Ekerfelt, A. Persson, O. Lundh and E. Berrocal. *Simultaneous laser-driven x-ray and two-photon fluorescence imaging of atomizing sprays.* Optica **7**, 131 (2020).

89. D. Guénot, K. Svendsen, B. Lehnert, H. Ulrich, A. Persson, A. Permogorov, L. Zigan, M. Wensing, O. Lundh and E. Berrocal. *Distribution of Liquid Mass in Transient Sprays Measured Using Laser-Plasma-Driven X-Ray Tomography.* Physical Review Applied **17**, 064056 (2022).

90. J. Hsieh. *Computed Tomography: Principles, Design, Artifacts, and Recent Advances, Fourth Edition* (2022). SPIE. ISBN 9781510646872.

91. K. Svendsen, D. Guénot, J. B. Svensson, K. Petersson, A. Persson and O. Lundh. *A focused very high energy electron beam for fractionated stereotactic radiotherapy.* Scientific Reports **11**, 5844 (2021).

92. J. J. Su, T. Katsouleas, J. M. Dawson and R. Fedele. *Plasma lenses for focusing particle beams.* Physical Review A **41**, 3321–3331 (1990).

93. C. Thaury, E. Guillaume, A. Döpp, R. Lehe, A. Lifschitz, K. Ta Phuoc, J. Gautier, J. P. Goddet, A. Tafzi, A. Flacco, F. Tissandier, S. Sebban, A. Rousse and V. Malka. *Demonstration of relativistic electron beam focusing by a laser-plasma lens.* Nature Communications 2015 6:1 **6**, 1–5 (2015).

94. R. Pompili, M. Anania, M. Bellaveglia, A. Biagioni, S. Bini, F. Bisesto, E. Brentegani, F. Cardelli, G. Castorina, E. Chiadroni, A. Cianchi, O. Coiro, G. Costa, M. Croia, D. Di Giovenale, M. Ferrario, F. Filippi, A. Giribono, V. Lollo, A. Marocchino, M. Marongiu, V. Martinelli, A. Mostacci, D. Pellegrini, L. Piersanti, G. Di Pirro, S. Romeo, A. Rossi, J. Scifo, V. Shpakov, A. Stella, C. Vaccarezza, F. Villa and A. Zigler. *Focusing of High-Brightness Electron Beams with Active-Plasma Lenses.* Physical Review Letters **121**, 174801 (2018).

95. J. van Tilborg, S. Steinke, C. Geddes, N. Matlis, B. Shaw, A. Gonsalves, J. Huijts, K. Nakamura, J. Daniels, C. Schroeder, C. Benedetti, E. Esarey, S. Bulanov, N. Bobrova, P. Sasorov and W. Leemans. *Active Plasma Lensing for Relativistic Laser-Plasma-Accelerated Electron Beams.* Physical Review Letters **115**, 184802 (2015).

96. R. Lehe, C. Thaury, E. Guillaume, A. Lifschitz and V. Malka. *Laser-plasma lens for laser-wakefield accelerators.* Physical Review Special Topics - Accelerators and Beams **17**, 121301 (2014).

97. S. Kuschel, D. Hollatz, T. Heinemann, O. Karger, M. B. Schwab, D. Ullmann, A. Knetsch, A. Seidel, C. Rödel, M. Yeung, M. Leier, A. Blinne, H. Ding, T. Kurz, D. J. Corvan, A. Sävert, S. Karsch, M. C. Kaluza, B. Hidding and M. Zepf. *Demonstration of passive plasma lensing of a laser wakefield accelerated electron bunch.* Physical Review Accelerators and Beams **19**, 071301 (2016).

98. N. Barov and J. B. Rosenzweig. *Propagation of short electron pulses in underdense plasmas.* **49** (1994).

99. B. Hidding, A. Beaton, L. Boulton, S. Corde, A. Doepp, F. A. Habib, T. Heinemann, A. Irman, S. Karsch, G. Kirwan, A. Knetsch, G. G. Manahan, A. Martinez de la Ossa, A. Nutter, P. Scherkl, U. Schramm and D. Ullmann. *Fundamentals and Applications of Hybrid LWFA-PWFA.* Applied Sciences **9**, 2626 (2019).

100. M. F. Gilljohann, H. Ding, A. Döpp, J. Götzfried, S. Schindler, G. Schilling, S. Corde, A. Debus, T. Heinemann, B. Hidding, S. M. Hooker, A. Irman, O. Kononenko, T. Kurz, A. Martinez De La Ossa, U. Schramm and S. Karsch. *Direct Observation of Plasma Waves and Dynamics Induced by Laser-Accelerated Electron Beams.* Physical Review X **9**, 011046 (2019).

101. A. M. De La Ossa, R. W. Assmann, M. Bussmann, S. Corde, J. P. Cabadag, A. Debus, A. Döpp, A. F. Pousa, M. F. Gilljohann, T. Heinemann, B. Hidding, A. Irman, S. Karsch, O. Kononenko, T. Kurz, J. Osterhoff, R. Pausch, S. Schöbel and U. Schramm. *Hybrid LWFA-PWFA staging as a beam energy and brightness transformer: Conceptual design and simulations.* Philosophical Transactions of the Royal Society A: Mathematical, Physical and Engineering Sciences **377** (2019).

102. T. Kurz, T. Heinemann, M. F. Gilljohann, Y. Y. Chang, J. P. Couperus Cabadağ, A. Debus, O. Kononenko, R. Pausch, S. Schöbel, R. W. Assmann, M. Bussmann, H. Ding, J. Götzfried, A. Köhler, G. Raj, S. Schindler, K. Steiniger, O. Zarini, S. Corde, A. Döpp, B. Hidding, S. Karsch, U. Schramm, A. Martinez de la Ossa and A. Irman. *Demonstration of a compact plasma accelerator powered by laser-accelerated electron beams.* Nature Communications 2021 12:1 **12**, 1–9 (2021).

103. W. Wang, K. Feng, L. Ke, C. Yu, Y. Xu, R. Qi, Y. Chen, Z. Qin, Z. Zhang, M. Fang, J. Liu, K. Jiang, H. Wang, C. Wang, X. Yang, F. Wu, Y. Leng, J. Liu, R. Li and Z. Xu. *Free-electron lasing at 27 nanometres based on a laser wakefield accelerator.* Nature **595**, 516–520 (2021).

104. M. Labat, J. C. Cabadağ, A. Ghaith, A. Irman, A. Berlioux, P. Berteaud, F. Blache, S. Bock, F. Bouvet, F. Briquez, Y.-Y. Chang, S. Corde, A. Debus, C. De Oliveira, J.-P. Duval, Y. Dietrich, M. El Ajjouri, C. Eisenmann, J. Gautier, R. Gebhardt, S. Grams, U. Helbig, C. Herbeaux, N. Hubert, C. Kitegi, O. Kononenko, M. Kuntzsch, M. LaBerge, S. Lê, B. Leluan, A. Loulergue, V. Malka, F. Marteau, M. H. N. Guyen, D. Oumbarek-Espinos, R. Pausch, D. Pereira, T. Püschel, J.-P. Ricaud, P. Rommeluere, E. Roussel, P. Rousseau, S. Schöbel, M. Sebdaoui, K. Steiniger, K. Tavakoli, C. Thaury, P. Ufer, M. Valléau, M. Vandenberghe, J. Vétéran, U. Schramm and M.-E. Couprie. *Seeded free-electron laser driven by a compact laser plasma accelerator.* Nature Photonics **17**, 150–156 (2023).

105. J. Ferri, V. Horný and T. Fülöp. *Generation of attosecond electron bunches and x-ray pulses from few-cycle femtosecond laser pulses.* Plasma Physics and Controlled Fusion **63** (2021).

106. X.-L. Zhu, M. Chen, S.-M. Weng, T.-P. Yu, W.-M. Wang, F. He, Z.-M. Sheng, P. McKenna, D. A. Jaroszynski and J. Zhang. *Extremely brilliant GeV γ-rays from a two-stage laser-plasma accelerator.* Science Advances **6** (2020).

107. M. Kozlova, I. Andriyash, J. Gautier, S. Sebban, S. Smartsev, N. Jourdain, U. Chulagain, Y. Azamoum, A. Tafzi, J. P. Goddet, K. Oubrerie, C. Thaury, A. Rousse and K. Ta Phuoc. *Hard X Rays from Laser-Wakefield Accelerators in Density Tailored Plasmas.* Physical Review X **10**, 011061 (2020).

108. K. Svendsen, I. Gallardo González, M. Hansson, J. B. Svensson, H. Ekerfelt, A. Persson and O. Lundh. *Optimization of soft X-ray phase-contrast tomography using a laser wakefield accelerator* (2018).

109. H. Legall, H. Stiel, M. Schnürer, M. Pagels, B. Kanngießer, M. Müller, B. Beckhoff, I. Grigorieva, A. Antonov, V. Arkadiev and A. Bjeoumikhov. *An efficient X-ray spectrometer based on thin mosaic crystal films and its application in various fields of X-ray spectroscopy.* J. Appl. Cryst **42**, 572–579 (2009).

110. J. Björklund Svensson, D. Guénot, J. Ferri, H. Ekerfelt, I. Gallardo González, A. Persson, K. Svendsen, L. Veisz and O. Lundh. *Low-divergence femtosecond X-ray pulses from a passive plasma lens.* Nature Physics **17**, 639–645 (2021).

111. H. T. Kim, K. H. Pae, H. J. Cha, I. J. Kim, T. J. Yu, J. H. Sung, S. K. Lee, T. M. Jeong and J. Lee. *Enhancement of Electron Energy to the Multi-GeV Regime by a Dual-Stage Laser-Wakefield Accelerator Pumped by Petawatt Laser Pulses.* Physical Review Letters **111**, 165002 (2013).

112. A. D. Andres, S. W. Jolly, P. Fischer, P. Fischer, A. A. Muschet, F. Schnur and L. Veisz. *Spatio-spectral couplings in optical parametric amplifiers.* Optics Express, Vol. 31, Issue 8, pp. 12036-12048 **31**, 12036–12048 (2023).

113. A. Popp, J. Vieira, J. Osterhoff, Z. Major, R. Hörlein, M. Fuchs, R. Weingartner, T. P. Rowlands-Rees, M. Marti, R. A. Fonseca, S. F. Martins, L. O. Silva, S. M. Hooker, F. Krausz, F. Grüner and S. Karsch. *All-optical steering of laser-wakefield-accelerated electron beams.* Physical Review Letters **105**, 215001 (2010).

114. D. E. Mittelberger, M. Thévenet, K. Nakamura, A. J. Gonsalves, C. Benedetti, J. Daniels, S. Steinke, R. Lehe, J. L. Vay, C. B. Schroeder, E. Esarey and W. P. Leemans. *Laser and electron deflection from transverse asymmetries in laser-plasma accelerators.* Physical Review E **100**, 063208 (2019).

115. F. Albert, M. E. Couprie, A. Debus, M. C. Downer, J. Faure, A. Flacco, L. A. Gizzi, T. Grismayer, A. Huebl, C. Joshi, M. Labat, W. P. Leemans, A. R. Maier, S. P. Mangles, P. Mason, F. Mathieu, P. Muggli, M. Nishiuchi, J. Osterhoff, P. P. Rajeev, U. Schramm, J. Schreiber, A. G. Thomas, J. L. Vay, M. Vranic and K. Zeil. *2020 roadmap on plasma accelerators.* New Journal of Physics **23** (2021).

116. M. Fuchs, R. Weingartner, A. Popp, Z. Major, S. Becker, J. Osterhoff, I. Cortrie, B. Zeitler, R. Hörlein, G. D. Tsakiris, U. Schramm, T. P. Rowlands-Rees, S. M. Hooker, D. Habs, F. Krausz, S. Karsch and F. Grüner. *Laser-driven soft-X-ray undulator source.* Nature Physics **5**, 826–829 (2009).

117. L. Labate, D. Palla, D. Panetta, F. Avella, F. Baffigi, F. Brandi, F. Di Martino, L. Fulgentini, A. Giulietti, P. Köster, D. Terzani, P. Tomassini, C. Traino and L. A. Gizzi. *Toward an effective use of laser-driven very high energy electrons for radiotherapy: Feasibility assessment of multi-field and intensity modulation irradiation schemes.* Scientific reports **10** (2020).

118. A. R. Maier, N. Kajumba, A. Guggenmos, C. Werle, J. Wenz, N. Delbos, B. Zeitler, I. Dornmair, J. Schmidt, E. M. Gullikson, F. Krausz, U. Schramm, U. Kleineberg, S. Karsch and F. Grüner. *Water-Window X-Ray Pulses from a Laser-Plasma Driven Undulator.* Scientific Reports 2020 10:1 **10**, 1–8 (2020).

119. J. Faure, D. Gustas, D. Guénot, A. Vernier, F. Böhle, M. Ouillé, S. Haessler, R. Lopez-Martens and A. Lifschitz. *A review of recent progress on laser-plasma acceleration at kHz repetition rate.* Plasma Physics and Controlled Fusion **61**, 014012 (2018).

120. R. D'Arcy, J. Chappell, J. Beinortaite, S. Diederichs, G. Boyle, B. Foster, M. J. Garland, P. G. Caminal, C. A. Lindstrøm, G. Loisch, S. Schreiber, S. Schröder, R. J. Shalloo, M. Thévenet, S. Wesch, M. Wing and J. Osterhoff. *Recovery time of a plasma-wakefield accelerator.* Nature **603**, 58–62 (2022).

121. M. P. Tooley, B. Ersfeld, S. R. Yoffe, A. Noble, E. Brunetti, Z. M. Sheng, M. R. Islam and D. A. Jaroszynski. *Towards Attosecond High-Energy Electron Bunches: Controlling Self-Injection in Laser-Wakefield Accelerators Through Plasma-Density Modulation.* Physical Review Letters **119**, 044801 (2017).

122. D. Guénot, D. Gustas, A. Vernier, B. Beaurepaire, F. Böhle, M. Bocoum, M. Lozano, A. Jullien, R. Lopez-Martens, A. Lifschitz and J. Faure. *Relativistic electron beams driven by kHz single-cycle light pulses.* Nature Photonics 2017 11:5 **11**, 293–296 (2017).

Papers

Printed by Media-Tryck, Lund 2025 NORDIC SWAN ECOLABEL 3041 0903

Faculty of Engineering, LTH
Department of Physics

Lund Reports on Atomic Physics, LRAP 610 (2025)
ISBN 978-91-8104-513-0
ISSN 0281-2762